This is a preprint, the final version is subject to change, of the American Mineralogist (MSA)
Cite as Authors (Year) Title. American Mineralogist, in press.
DOI: https://doi.org/10.2138/am-2019-7011

Revision 2

High Pressure Raman and Nd^{3+} Luminescence Spectroscopy of Bastnäsite-(REE)CO_3F

C. E. Vennari,[1]* Q. Williams[1]

[1]Department of Earth and Planetary Sciences, University of California Santa Cruz, Santa Cruz, CA 95064, USA

Abstract

Bastnäsite-(Ce), a rare earth element (REE) bearing carbonate (Ce,La,Y,Nd,Pr)CO_3F, is one of the most common REE-bearing minerals, and has importance from both economic and geologic perspectives due to its large REE concentration. It also provides an example of the structural interplay between carbonate groups and fluorine ions, as well as the complex bonding properties of rare earth elements. We report Raman vibrational and Nd^{3+} luminescence ($^4F_{3/2}\rightarrow{}^4I_{9/2}$. $^4F_{3/2}\rightarrow{}^4I_{11/2}$ and $^4F_{5/2}+{}^2H_{9/2}\rightarrow{}^4I_{9/2}$) spectra of natural bastnäsite-(Ce) to 50 GPa at 300 K. Two phase transitions are observed under compression. Bastnäsite-I remains the stable phase up to 25 GPa, where it undergoes a subtle phase transition to bastnäsite-II. This is likely produced by a change in symmetry of the carbonate ion. Bastnäsite-II transforms to bastnäsite-III at ~38 GPa, as demonstrated by changes in the luminescence spectra. This second transition is particularly evident within the $^4F_{3/2}\rightarrow{}^4I_{9/2}$ luminescent transitions, and it appears that a new rare earth element site is generated at this phase change. This transition is also accompanied by modest changes in both the Raman spectra and two sets of luminescent transitions. Despite these transformations, the carbonate unit remains a stable, three-fold coordinate unit throughout this pressure range, with a possible increase in its distortion. Correspondingly, the rare-earth element site(s) appears to persist in quasi-9-fold coordination as well, implying that the general bonding

configuration in bastnäsite is at least metastable over a ~30% compression range. All pressure-induced transitions are reversible, with some hysteresis, reverting to its ambient pressure phase on decompression.

Keywords: Bastnäsite, high pressure, Raman spectroscopy, rare earth elements, neodymium luminescence spectroscopy, carbon, deep Earth

Introduction

Bastnäsite-(Ce) is a rare earth element (REE) bearing fluorocarbonate ($(Ce,La,Y,Nd,Pr)CO_3(F,OH)$) that is typically found associated with carbonatite deposits, and is economically important due to its high content of REEs. Indeed, bastnäsite is one of the two major mineral ores for REEs, with its chief competition being monazite. Geochemically, REEs are typically incompatible in silicate minerals; their concentration in carbonatite melts (often with bastnäsite as their crystallization product) is generally more than 3 orders of magnitude higher than the bulk Earth content (Jones et al. 2013), and greater than 4 orders of magnitude higher than within chondrites (Holtstam and Andersson 2007). Indeed, carbonate-bearing liquids and solids likely play a primary role in transporting and retaining rare earth elements within the Earth's mantle (e.g., Collerson et al. 2010). In addition, light REE have long been used to determine the ages of continental rocks, particularly via the samarium-neodymium dating method (McCulloch and Wasserburg 1978), and the evolution of the depleted mantle has been probed using the distinct $^{143}Nd/^{144}Nd$ variation in the mantle compared to chondrites and crustal rocks (DePaolo and Wasserburg 1976). Bastnäsite has significance beyond its REE content: as carbonates are thought to be the dominant species containing carbon within oxidized regions of the mantle (e.g., Brenker et al. 2007), the properties of bastnäsite can provide insight into the bonding of carbon at depth. Specifically, bastnäsite, has importance for understanding the

potential behavior of REE at depth within carbon (and halogen) enriched zones of the mantle, and within carbonatite melts (which are frequently halogen-enriched: e.g., Jago and Gittins 1991; Williams and Knittle 2003). Additionally, the optical and magnetic properties of rare-earth carbonate fluorides have attracted interest within the materials science community (e.g., Grice et al. 2007).

Bastnäsite virtually never occurs as an endmember in terms of its REE content, as it commonly contains a mixture of REEs (e.g. Ce, Nd, Eu, Y, etc.). Visible and infrared reflectance spectroscopy have been used to probe the absorption bands of bastnäsite, which can constrain the REE content (Turner et al. 2015); however, assignments to the absorptions and energy levels of different REEs have generally not been made to the observed absorption peaks. In addition, the rare earths in bastnäsite luminesce strongly; as discussed below, it appears that this fluorescence has at times been associated with hydroxyl stretching vibrations in Raman spectroscopic experiments (Frost and Dickfos 2007). In this study, we are able to assign the luminescence peaks to transitions of the neodymium ion, and probe changes to the REE site with pressure by using this Nd^{3+} luminescence.

Luminescence has been employed extensively as a probe for pressure-induced changes in crystal structure or in electronic configuration (e.g., Dolan et al. 1986; Freire et al. 1994; Bray 2001; O'Bannon and Williams 2016). Neodymium luminescence has been investigated for use as a pressure calibrant due to its high fluorescence intensity and insensitivity to changes in temperature (e.g., Hua et al. 1996), with $YAlO_3$ being typically viewed as the most promising Nd-bearing sensor due to its lack of phase change or amorphization up to 80 GPa (Hua and Vohra 1997; Hernández-Rodríguez et al. 2018a, 2018b). Other high pressure studies using Nd^{3+} luminescence have investigated the pressure-shifts of different energy levels and their associated

crystal field parameters (e.g., Santiuste et al. 2017; Hernández-Rodríguez et al. 2018a). Thus, Nd^{3+} luminescence has been investigated under pressure in a range of oxide crystals to derive insights into the electronic properties of crystals used for solid state lasers under compression, and at ambient pressure within minerals (e.g., Lenz et al. 2013). However, to our knowledge, high-pressure Nd^{3+} luminescence spectroscopy has not been previously utilized to probe the electronic and structural changes within a geologically relevant mineral. Here, we employ both Raman and Nd^{3+} luminescence spectroscopy to constrain changes in the bonding environments of both the carbonate and neodymium ions in bastnäsite; this is the first high pressure study of bastnäsite using these complementary techniques.

Experimental Methods

Natural bastnäsite $(Ce_{0.49}La_{0.25}Nd_{0.21}Pr_{0.04})CO_3(F_{0.95}(OH)_{0.05})$ from Northern Pakistan was used for these experiments. The chemical composition of the sample was confirmed with four grains of bastnäsite using a Thermoscientific Apreo scanning electron microscope equipped with an Oxford Instruments Ultim Max 100 mm energy dispersive X-ray spectrometer (0.8 nA and 15kV beam); SEM results are shown in Table S1 and Fig. S1 . Raman spectroscopy and single crystal X-ray diffraction of this sample were in excellent agreement with previous determinations (Ni et al. 1993; Frost and Dickfos 2007).

The ambient pressure crystal structure was measured at beamline 12.2.1 at the Advanced Light Source. Diffraction images were collected at 100 K with a Bruker D8 diffractometer equipped with a Photon II CPAD detector, and X-rays monochromated by silicon (111) to 17 keV (0.7288 Å). The single crystal was a clear block that was free of visible cracks and/or imperfections, with an approximate size of 90 x 80 x 50 μm. The sample was mounted in Paratone-N oil on a MiTeGen Micromount. Diffraction images were collected using the APEX3

93 program (Bruker 2016a). Images were integrated and cell refinements were computed using
94 SAINT V8.34A (Bruker 2013). The sample symmetry of the ambient structure was determined
95 using XPREP, and crystal absorption was corrected using the algorithms of SADABS-2016/2
96 (Bruker 2016b). The crystal structure from Ni et al. (1993) was used as an initial fit, and refined
97 using full-matrix least-squares on F^2 via SHELXL-2018/1 (Sheldrick 2015), using the software
98 package ShelXle Rev 806 (Hübschle et al. 2011).
99 Raman and luminescence spectra were collected using a Horiba LabRam HR Evolution
100 spectrometer equipped with either a 633 or 532 nm excitation laser, depending on the experiment
101 being conducted. The spectrometer focal length was 800 mm, and a grating of 1800 lines/mm
102 was used with a spectral resolution of ~1 cm^{-1}. Spectra were collected up to a pressure of ~50
103 GPa at ~300 K. Peak positions were calculated from fits that used a combination of Gaussian and
104 Lorentzian peak shapes with Horiba LabSpec6 software.
105 High pressures were generated using a Princeton type symmetric diamond anvil cell
106 equipped with type IIa diamonds with 250 μm culets. Rhenium was used as the gasket material.
107 Gaskets were preindented to ~30 μm thickness, and the sample compartments were ~125 μm in
108 diameter. Neon was used as a pressure medium, as it is closer to hydrostatic than most other
109 pressure media at high pressures (Klotz et al. 2009); however, supplementary data were collected
110 using a 4:1 methanol:ethanol pressure medium, as reported in Fig. S2. These are completely
111 consistent with the data reported here in a neon medium. . Ruby fluorescence from multiple ruby
112 grains within the sample compartment was used to both determine pressures, and pressure
113 variations within the chamber (Dewaele et al. 2008): our results are compatible with those of
114 Klotz et al. (2009) in there being an order of a few tenths of GPa of pressure variations at the
115 highest pressures of these measurements.

Results

The ambient pressure, low temperature crystal structure (Fig. 1) of our sample agrees with the previously reported structure by Ni et al. (1993), rather than with the structure inferred by Donnay and Donnay (1953). Bastnäsite is in the space group *P*-62*c*, with a = 7.0838(2) Å, c = 9.7365(3) Å, and 6 formula units in the unit cell. Its structure has alternating layers comprised of $(CO_3)^{2-}$ units and REE ions juxtaposed with F ions in the *c*-axis direction (Fig. 1). The REE atoms are in a 9-coordinate site (with a volume of 31.338 $Å^3$), with a point symmetry of C_2. The atoms comprising the REE polyhedra are 3 fluorine atoms and 6 oxygen atoms. There is one carbonate group within the unit cell; the carbon and one of its coordinating oxygens (O1) lie on a mirror plane, and the other oxygens (O2) in the carbonate group are related by symmetry. The C-O1 distance is 1.2901(45) Å and C-O2(x2) are 1.2845(27) Å and the carbon atom lies (within error) in a plane with the three oxygen atoms (0.0024(27)) Å out of the plane generated by the three oxygen atoms). There are two fluorine atom sites within the unit cell; F1 lies (roughly) in a plane with the REE atoms that generate a plane at x~0.66. F2 lies out of this plane, causing a distortion of the REE polyhedra.

At ambient pressure and temperature, thirteen lattice modes and seven modes associated with the carbonate ion are resolved in the Raman spectrum (Fig. 2a). There are a large number of modes in the lattice region of the ambient spectrum, reflecting the relatively low symmetry of the polyhedra of the REE ions, with bonding to both oxygen and fluorine. The modes associated with the carbonate ions are easily assigned: the symmetric stretch (ν_1) is at 1,096 cm^{-1}, one mode associated with the out-of-plane bend (ν_2) is at 870 cm^{-1}, an asymmetric stretch (ν_3) is at 1432 cm^{-1}, and the in-plane bend (ν_4) has components at 664, 686, 729, and 737 cm^{-1}. The increased number of carbonate modes compared to the isolated ion is due to the distortion of the carbonate

ion coupled with its low symmetry site within the crystal structure. Factor group analysis of the optic modes of bastnäesite with the space group *P*-62*c*, yields:

$$\Gamma_{optic} = 9A'_1 (R) + 7A''_1 (Inactive) + 11A'_2 (Inactive) + 8A''_2 (IR) + 19E' (R,IR) + 16 E'' (R) .$$

Thus, there are 44 Raman active vibrations and 27 infrared active vibrations; accordingly, the numbers of anticipated Raman active modes and carbonate modes are substantially greater than we observe, which is not unusual given that both weak modes and accidental degeneracies are typically present in complex, low-symmetry molecular crystals. At high pressures, splittings and mode discontinuities in the Raman data provide *prima facie* evidence for phase transitions that occur under compression.

Bastnäsite does not naturally occur as the pure endmember with a given rare earth element, so multi-element occupancy of the rare earth element site is expected. In our bastnäsite sample, neodymium substitutes at the 24% level into the REE site. As such, we probe the Nd^{3+} luminescence within the structural environment of the REE site (Fig. 2b), and monitor systematic changes in city distortion via the luminescence spectroscopy. Within the bastnäsite crystal structure, neodymium's electronic energy levels are split by three principal effects: (1) by electrostatic interactions, (2) spin orbit coupling, and (3) the local electric field that generates 2 to 6 Stark components (depending on the energy level), as imposed by the crystal field surrounding the ion (Fig. 3). The observed Nd^{3+} luminescence is entirely consistent with that of a Nd^{3+} ion in a site with low symmetry (e.g., Table 4.3 of Kaminskii 1981). We observe luminescence associated with energy transitions between these electronic states: $^4F_{5/2}+^2H_{9/2} \rightarrow {}^4I_{9/2}$ at ~790-822 nm, $^4F_{3/2} \rightarrow {}^4I_{9/2}$ at ~862-900 nm, and $^4F_{3/2} \rightarrow {}^4I_{11/2}$ at ~1046-1066

nm (Fig. 3). We are able to deconvolve the peaks and assign the energy levels of each Stark-split level ($^4I_{9/2}$, $^4I_{11/2}$, $F_{3/2}$, $^4F_{5/2}$, $^2H_{9/2}$) of the spin orbit coupled energy levels (Fig. 2b).

High Pressure Raman Results and Discussion

Bastnäsite-I: Raman spectroscopy under pressure

We resolve mode shifts for both lattice and carbonate modes of the ambient pressure phase of bastnäsite up to 25 GPa (Fig. 4). Mode assignments and their pressure shifts are reported with associated mode Grüneisen parameters in Table 1, calculated using the bulk modulus of 105 GPa from Rowland (2017). Below 25 GPa, the lattice modes all increase in frequency with pressure, with no major changes in their number or peak shape morphology (Fig. 4a, d). Some apparent changes in intensity are observed in this pressure range, but these changes are likely due to a combination of pressure-induced removal of accidental degeneracies and possible effects of changes in crystal orientation between different spectra.

The Raman active modes of the carbonate ion shift monotonically up to 25 GPa, indicating that no phase change occurs up to this pressure. The symmetric stretching mode (ν_1) shifts approximately linearly up to 25 GPa at a rate of 2.79 cm^{-1}/GPa. Interestingly, at ambient pressure, this peak is more asymmetric than at 23 GPa. The carbonate out-of-plane bend (ν_2) shifts negatively at -0.29(8) cm^{-1}/GPa; such a modest negative shift is typical for carbonate minerals (e.g., aragonite and dolomite: Kraft et al. 1991; Vennari and Williams 2018). This mode grows in intensity on compression compared to the in-plane bend, and at 25 GPa, the mode has twice its relative amplitude as at lower pressures. This shift in intensity is plausibly associated with a Fermi resonance between higher-lying components of the ν_4 in plane bend and the ν_2 out-of-plane bend, as these bands approach one another under pressure (their separation changes from ~130 cm^{-1} to near 75 cm^{-1} at 25 GPa: Fig. 4b).

The four carbonate in-plane bends (ν_{4a}, ν_{4b}, ν_{4a}, ν_{4b}) all shift positively with pressure (Fig. 4b,d, Table 1), and their relative intensities also shift with pressure. The highest frequency band (ν_{4d}) remains the most intense up to 25 GPa. The second highest frequency mode (ν_{4c}), which initially is present as a shoulder, merges into the highest frequency band under pressure, and may decrease in relative amplitude: we believe this decrease may be from a combination of a compression-induced loss of Fermi resonance, coupled with a peak broadening of the most intense peak. There appears to be a general increase in relative intensity of the third-highest frequency in-plane bending mode with pressure (ν_{4b}), although the intensities of the two lowest frequency in-plane bending modes (ν_{4a}, ν_{4b}) relative to one another appear largely unchanged under compression. The pressure shifts of the two lower frequency bending modes (ν_{4a}, ν_{4b}) are such that they diverge from the two highest frequency in-plane bending modes (ν_{4c}, ν_{4d}), implying that the distortion of the carbonate group may increase under compression in bastnäsite.

Bastnäsite-II: Raman spectroscopy under pressure

The phase change that occurs at 25 GPa is primarily manifested by changes of the carbonate vibrations, although there are some shifts in the lattice region, as well (Fig. 4). Most lattice modes appear to persist through this phase change: however, three new low intensity modes appear at 284, 430 and 480 cm^{-1}. Within the carbonate region, the symmetric stretch splits (Fig. S4), with a second peak appearing on its lower frequency side; this splitting is first resolved through deconvolution near 25 GPa (Fig. S4), but becomes progressively more pronounced as pressure is increased. The two highest frequency in-plane bends (ν_{4c}, ν_{4d}), which below 25 GPa progressively merge into a single peak, become a single, asymmetric peak. The other two in-plane bend modes (ν_{4a}, ν_{4b}) and the out-of-plane bend mode each increase in intensity across the

transition (Fig. 4). Taken together, these changes are consistent with a change in symmetry of the carbonate group, probably from *m* to lower symmetry.

The pressure shifts of the lattice modes in bastnäsite-II are listed in Table 2, and shown in Fig. 4a,c. In addition to the modes that first are resolved at 25 GPa, there are two weak modes that become unresolvable at this pressure (those with zero pressure frequencies of 140 and 185 cm^{-1}). Relative to the carbonate region, these are relatively subtle changes in the lattice region of the Raman spectrum. Accordingly, the REE site within bastnäsite-II has likely only changed modestly compared to bastnäsite-I; certainly, no shift in coordination of the REE site occurs. The lowest frequency lattice mode splits at 30 GPa—we believe that this may be due to pressure-induced elimination of an accidental degeneracy rather than the phase change itself, as no other lattice modes split at the same pressure. The new intermediate frequency mode (at 284 cm^{-1} at the transition) is only readily tracked until the transition to bastnäsite-III at 38 GPa. Overall, the lattice modes undergo remarkably little alteration with pressure; the two higher frequency lattice modes that appear at 25 GPa are resolvable to the highest pressure probed. This persistence of many of the lattice modes suggests that the topological changes that occur at the two phase transitions do not profoundly affect the lattice vibrations (which are likely more associated with the REE-F layer within the structure and vibrations of the rare earth elements against the carbonate framework). It is possible that a coexistence of multiple REE sites, with different distortions but similar coordination, occurs in the pressure range from 25 GPa to 38 GPa.

The pressure shifts of the modes (ν_1, ν_{1a}) associated with the symmetric stretch of the carbonate ion decrease above 25 GPa, and, as pressure is increased, the two modes associated with the symmetric stretch in the high-pressure phase separate in frequency. Notably, the lower frequency in-plane bend (ν_{2b}) and the out-of-plane bending (ν_2) vibrations become sharper after

the transition at 25 GPa to bastnäsite-II up until 38 GPa: this may be a consequence of the transition relieving internal stress within the crystal. Nevertheless, even though there is a change in intensity and shape of a subset of the carbonate bending modes across the transition, there is neither a change in the observed number of peaks, nor a discontinuous change in their frequencies. Bastnäsite-II may have more distorted cation sites (due to the larger number of lattice peaks observed), but does not have major changes associated with its bonding, nor an apparent doubling of sites within the unit cell. The most marked effect of the transition is the splitting of the symmetric stretching vibration (ν_1, ν_{1a}) of the carbonate group, implying that the local symmetry of the carbonate group may have shifted.

Bastnäsite-III: Raman spectroscopy under pressure

The transition from bastnäsite-II to –III is marked by further splitting of the carbonate modes and modest changes in the lattice modes near 38 GPa. Again, additional modes split at this transition, and there are significant changes in band intensities: for example, the most intense lattice mode at ~390 cm^{-1} at 38 GPa becomes markedly less intense compared to the other modes. It is unclear whether this transition, which clearly initiates at 38 GPa, is complete near this pressure, or whether it is kinetically impeded, and occurs gradually across a wide pressure range. The net decline in intensity of a number of the vibrational modes of bastnäsite-II between 38 and 51 GPa, and apparent growth of new, or weak, bands is compatible with the latter interpretation. If, however, this is a transition that is complete near 38 GPa, the new modes (at 120 and 271 cm^{-1}) that appear at the transition indicate that either the REE site is further distorted, and/or there has been a doubling of the REE sites within the unit cell. We believe, in conjunction with the luminescence data described below, that a new REE site is produced associated with the transition to bastnäsite-III.

The changes of the carbonate vibrations at the transition to bastnäsite-III are more dramatic than those associated with the bastnäsite-I to –II transition. The symmetric stretch, which splits into two deconvolvable modes (ν_1, ν_{1a}) above 25 GPa, requires a new component (ν_{1b}) to fit its band shape above 38 GPa (Fig. 4c). The out-of-plane bend begins to become asymmetric at 36 GPa, and splits from one band to three distinct modes (ν_2, ν_{2a}, ν_{2b}) above 38 GPa. The highest frequency in-plane bending peak (ν_{4d}) sharpens across the transition to bastnäsite-III; the two components (ν_{4c}, ν_{4d}) of this peak become difficult to deconvolve above 38 GPa. The next highest frequency in-plane bending peak (ν_{4b}) remains sharp and distinct across the transition, but a change in its peak shape is apparent: the top of the peak remains sharp, but the bottom broadens, and there may be additional, not-readily-resolved modes on its high and low frequency sides. Accordingly, two of the three (and possibly all three) of the different types of carbonate vibrations monitored have additional bands that appear following the transition at 38 GPa.

The Raman spectrum of bastnäsite-III reflects both distorted carbonate ions and potentially multiple REE sites that persist to the highest pressures probed (52 GPa). While Raman spectroscopy is an excellent probe for characterizing changes in local bonding environments, we supplement these results with Nd^{3+} luminescence results to characterize the electronic transitions of Nd in the REE site in order to better constrain structural changes that specifically involve the REE ion.

High Pressure Nd^{3+} Luminescence Results and Discussion

Figures 5-7 show both our luminescence results within different spectral regions, and the ambient pressure energy level diagrams for the associated transitions. In each instance, we use the peak nomenclature of Dieke (1969). The majority of the transitions have red shifts of their

respective luminescence with pressure – such an approach of long-lived luminescing electronic states towards the ground state under compression is common, such as for Nd^{3+} in garnets (Hua et al. 1996) and Cr^{3+} in ruby (Mao et al. 1986), although exceptions exist (e.g., Hua and Vohra 1997; Hernández-Rodríguez et al. 2018a). The most intense and highest energy bands associated with the transition between the $^4F_{3/2}$ state and the $^4I_{9/2}$ ground state (which are, by convention, named R1 and R2: Dieke 1969), do not redshift or blueshift notably; while they may have a small and non-linear pressure dependence, they shift little with pressure up to 50 GPa (Fig. 5). Thus, the pressure-induced shifts of the $^4F_{3/2}$ states are similar to that of the lowest energy $^4I_{9/2}$ state.

Overall, the luminescence changes subtly at the transition between bastnäsite-I and –II compared to the changes that occur across the bastnäsite-II to –III transition; this is likely due to the subtle nature of the first transition, and a more dramatic change in the REE site in the second transition (possibly involving a doubling of the number of REE sites in the cell). We discuss each of the major transition manifolds in sequence, since each show somewhat different behavior under compression.

$^4F_{3/2}$→$^4I_{9/2}$ luminescence under pressure

We observe all 10 peaks associated with the transitions between the Stark levels for the $^4F_{3/2}$ and $^4I_{9/2}$ states. The R1 and R2 bands provide a direct measure of the excited state ($^4F_{3/2}$) energy above the ground state. Under pressure, up until ~15 GPa, we see a decrease in their peak separation (Fig. 8). However, near 15 GPa this trend reverses, and the peaks begin to separate. Because the Stark splitting is produced by the local electric field at the Nd ion, this turnover is associated with an initial decrease in the electric field gradient, followed by an increase, or an onset of a more anisotropic local bonding environment. Such a change may be indicative of a

change in local bonding, and hence a shift in compressional behavior within the REE site, but does not necessarily indicate any change in crystal symmetry. The relative intensities of these bands remain relatively unchanged to 25 GPa.

From 25 to 38 GPa, most of the luminescence peak positions continue to decrease in energy at rates similar to those prior to the transition to bastnäsite-II; a representative spectrum at 31.2 GPa is peakfit in Fig. S5a. Interestingly, only one transition clearly increases in energy above 25 GPa: R2→Z2(3). This anomalous shift indicates that the splitting of the $^4I_{9/2}$ state is complex under compression, and that the electric field that is impacting the f-orbitals is anisotropic in its shape.

Above 38 GPa, many of the pairs of luminescence bands induced by the two $^4F_{3/2}$ states split from two to three or four peaks: this splitting strongly suggests that an additional rare earth element site is present within the unit cell of bastnäsite-III, consistent with our Raman spectra, with the new site having a modestly different set of Stark splittings. The number of Stark levels is capped by the low symmetry of the REE site—so any decrease in symmetry of the single REE site would not increase the number of peaks observed (Kaminskii 1981). Thus, the most plausible mechanism for producing additional bands is via the onset of a new REE site within the structure. Above 38 GPa, deconvolution of the luminescence bands and the presence of the new bands provide primary evidence for a new electronic environment within the structure; a representative deconvolved spectrum is shown in Fig. S6a. While we are able to determine the new R1 and R2 energy levels of the new site, we are unable to identify the new site's Z3 level. We believe this is due to the low intensity of the transitions from R1 and R2 to Z3 before the phase transition; thus, after the transition it remains difficult to determine the full suite of peak locations associated with the new site.

Interestingly, a new band begins to appear at the highest energies of this suite of transitions (associated with an additional transition from R2→Z1) near 36 GPa—this is likely either a precursor to, or the first indication of the phase change that we observe in the Raman spectra at 38 GPa. The intensity of the peak associated with R1→Z2(4) becomes more intense in bastnäsite-III. The change in intensity indicates that the excitation and/or emission cross sections for those transitions have changed: since we have not measured excitation spectra, we cannot distinguish which (or both) of these alternatives is the case.

$^4F_{3/2}$→$^4I_{11/2}$ luminescence under pressure

At room pressure and temperature using 532 nm excitation wavelength, we are able to also observe all 12 peaks associated with the transitions from the $^4F_{3/2}$ to $^4I_{11/2}$ states (Figure 6). At ambient pressure, the most intense peak is associated with the transition from R1→Y2 (14). The relative intensities of the respective peaks associated with transitions between these states is similar to that of Nd^{3+} in yttrium aluminum garnet, with the most intense being peak 14, with generally comparable intensities of the nearby lower amplitude peaks (e.g., Pokhrel et al. 2012). Figure 6 shows the changes produced by pressure, and Table 5 contains the pressure shifts of the peaks. Interestingly, the highest wavelength peaks (lowest energy transitions) associated with R1 and R2→Y5 and Y6 are not observable with 633 nm excitation—they were only observable with 532 nm excitation (Figure S3). We attribute this to the existence of either rapid non-radiative decay pathways associated with the absorptions that are pumped by the lower energy excitation, or those lower energy transitions being accessible when the higher energy transitions are overpopulated.

Under compression, all modes shifted to lower energy with increased pressure, and as with the $^4I_{9/2}$ transitions, the modes with the lowest 1-bar energy exhibited the strongest negative

pressure dependence. The lowest energy mode (18) becomes unresolvable above 15 GPa. Around this pressure, an additional peak 13* is observed at slightly lower energy than peak 13. These changes in peak position and intensity may be associated with the change in the sign of the trend of electric field near this pressure that is observed in the R2-R1 separation (Figure 8). At 25 GPa, peak 13 becomes unresolvable, and this shift may be associated with the transition from bastnäsite-I to -II. Overall, across the bastnäsite-I to -II transition, there are no major changes in either the number of luminescence peaks or their intensities, thus confirming our inference from the Raman spectra that this transition likely involves (at most) a subtle change to the REE site. Moreover, the pressures shifts of all bands are consistent in their migration to lower energy, indicating that these transitions may be less sensitive to changes in the detailed electric field gradient.

Above 25 GPa, the peaks associated with bastnäsite-II continue to broaden and decrease in intensity. As pressure is increased, peak 14 decreases particularly in intensity relative to the other bands in this multiplet. All peaks, except peak 16 (which becomes unresolvable) persist to 38 GPa; a representative spectrum at 31.2 GPa is peakfit in Fig. S5b.

Above 38 GPa, the relative intensities of individual peaks continue to change. As pressure is increased, the lower energy transitions become less intense relative to the higher energy transitions; specifically, peak 14, which at ambient pressure is the most intense, becomes the third most intense, following peaks 12 and 13. These intensity changes may be due to a splitting of peak 14. At 38 GPa, a lower energy peak branches off of peak 14. This splitting, coupled with the overall drop in intensity of the multiplet of peaks, further indicates that there is likely an additional, distinct REE site in the unit cell above 38 GPa; the deconvolution of a representative spectrum at 50.6 GPa is shown in Fig. S6b.

$^4F_{5/2}+^2H_{9/2}\rightarrow{}^4I_{9/2}$ luminescence under pressure

At ambient pressure and temperature, we observe seven peaks associated with the transition from $^4F_{5/2}+^4H_{9/2}\rightarrow{}^4I_{9/2}$. There is a well documented overlap between the energy levels of $^4F_{5/2}$ and $^4H_{9/2}$ (5 in $^4H_{9/2}$ and 3 in $^4F_{5/2}$), and identification of the individual Stark levels of the $^4F_{5/2}+^4H_{9/2}$ transitions to the $^4I_{9/2}$ state is helped by the fact that these transitions happen solely to the lowest energy state in $^4I_{9/2}$ (e.g., Muñoz Santiuste et al. 2017). Additionally, we are able to separate and identify the majority of the individual Stark levels due to differences in intensity, line shape and line width in both sets of transitions (Henderson et al. 1967). Once compressed above ~1 GPa, a fifth band associated with the transition from $^4H_{9/2}\rightarrow{}^4I_{9/2}$ is observed (Fig. 7). As an aside, we note that the appearance of this sequence of luminescence bands is essentially indistinguishable in both amplitude and absolute position (laser frequency minus reported Raman frequency) from bands that have been attributed to Raman-active hydroxyl stretching vibrations observed under 633 nm excitation in bastnäsite from Pakistan (Frost and Dickfos 2007).

Around 2 GPa, the pressure-induced removal of accidental degeneracies in the higher energy transitions becomes apparent, and the appearance of new bands continues as pressure is increased in bastnäsite-I. For example, the intensity of peak 25 decreases,likely also from the loss of degeneracy. As with most other emission bands in this system, the nine bands associated with these transitions all shift to lower energy with pressure up to 25 GPa (Fig. 7).

Above 25 GPa, two new bands emerge, and the highest energy mode 23 undergoes an anomalous shift to higher energy with pressure from 25 to 38 GPa. This shift is consistent with the changes in the highest-lying bands associated with the $^4F_{3/2}\rightarrow{}^4I_{9/2}$ transitions. All other peaks shift to lower energy with pressure until 38 GPa; a representative deconvolved spectrum at 31.2 GPa is shown in Fig. S5c.

Bastnäsite-III has broader and lower intensity luminescence peaks for this set of transitions (Fig. 7). This drop in intensity and increase in breadth is consistent with there being an additional REE site within the unit cell of this phase, but resolution of a separate full manifold of bands associated with the new site is not feasible. In addition to the intensity changes, there are discontinuous changes in some of the bands. For example, the lowest energy peak 30 becomes unresolvable above the transition, peak 25 shifts discontinuously to a higher energy, and a new band, (peak 26a**), branches out from between peaks 26a and 26a* (Fig. 7, Table 6); the deconvolution of the highest pressure spectrum is shown in Fig. S6c. As with the other luminescent sets of transitions, the higher pressure phase change involves more marked changes in the spectra than the lower pressure transition from bastnäsite-I to -II.

R1-R2 separation

The energy differences between the R1 and R2 bands are perhaps most readily associated with structural changes in the REE site under pressure (Figure 8). While the absolute shift of each energy level with pressure is quite small (Figure 5), the separation in energy between these two bands does change. An increase in energy separation is characteristic of a REE site that is decreasing in symmetry/increasing in distortion, and a decrease indicates the converse: a transition towards higher symmetry/lower distortion (e.g., Hua et al. 1996). From 0 to 15 GPa, the difference between these two modes initially decreases indicating a REE site that is becoming more symmetric or, in other words, R1 and R2 are becoming closer to degenerate (Fig. 8). At 15 GPa, the difference between these two energy levels increases with pressure until 25 GPa, thus indicating that the REE site is becoming more distorted. Above 25 GPa, the change in energy level separation is negligible until 38 GPa, where the onset of a new REE site occurs. The energy level splitting of the new and old REE site differ dramatically. The most striking change

is the energy difference between R1 and R2: at 50 GPa, the difference between R1 and R2 in the original REE site is ~42 cm^{-1}, and in the new site, the difference is ~96 cm^{-1}. While this difference is large, an energy difference between R1 and R2 of above 100 cm^{-1} is common within ambient pressure, highly distorted Nd^{3+} sites. For example, the R2-R1 separation is 123 cm^{-1} in CAZGAR ($CaZn_2Y_2Ge_3O_{12}$: Sardar and Yow 1998) and 116 cm^{-1} in $CaY_2MgGe_3O_{12}$ (Sharp et al. 1974). In addition, if site distortion increases under pressure, increased separation is expected, so this doubling of the R2-R1 separation in the new site to nearly 100 cm^{-1} is not outside the bounds of sites observed at ambient pressure in other phases.

Separation of energy levels with pressure

Over most of the pressure range (15-50 GPa) of this experiment, the luminescence bands within each set of transitions separate under compression, indicating a progressive increase in the crystal field splitting, which is likely associated with a pressure-induced increase in the distortion of the REE site. The change in the separation energy of $^4I_{9/2}$ (Z1-Z5) is 6.03 cm^{-1}/GPa, $^4I_{11/2}$ (Y1-Y4), is 3.61 cm^{-1}/GPa, $^4F_{3/2}$ (R1-R2) is 0.32 cm^{-1}/GPa, $^4F_{5/2}$ is 2.81 cm^{-1}/GPa, and $^2H_{9/2}$ is 3.63 cm^{-1}/GPa. Figure 9 displays the overall splitting of the spin orbit coupling energy levels, with the barycenters (the arithmetic means) shown as the energy levels (for all but the ground state). Similar rates of changes in the separation of the energy levels $^4I_{9/2}$, $^4I_{11/2}$, and $^4F_{3/2}$ have been observed previously in $YAlO_3$:Nd at high pressures (Hernández-Rodríguez et al. 2018a). Several distinct and separable effects are present in Figure 9. First, the net separation between the Stark levels of the ^2H, ^4F and ^4I levels decreases under compression. As shown in Figure 3, this indicates that the splitting of the f-levels induced by Coulombic splitting is reduced under compression. This implies that the interaction between f-orbitals is lessened, indicating that covalency of the REE site in bastnäsite increases under compression (this is a manifestation of an

increased nephelauxetic effect). The shift in Coulombic splitting can be semi-quantitatively assessed from Figure 9: the separations of the averages of the H, F, and I levels decrease by ~2% for both the H to I level differences and the F to I level differences between 0 and 40 GPa. The relative tradeoffs between a pressure-induced contraction in the size of the f-orbitals relative to decreased electron localization in these levels induced by increased covalency in generating this change in splitting by Coulombic repulsion are unclear. If, as an endmember upper bound on the maximum shift in electron occupancy, the entire shift in Coulombic splitting is attributed to a change in occupancy, then a decrease of ~1% in electron occupancy in the f-orbitals is indicated by the results of Figure 9: a relatively small, but spectroscopically significant, shift relative to the magnitude of the change in volume of the system (which is of order ~19% at 40 GPa using Rowland's (2017) bulk modulus value). In passing, we note that this semi-quantitative estimate, derived from luminescence spectra, could be rigorously tested via single-crystal diffraction constraints on the pressure-dependence of electron density distributions.

In terms of the spin-orbit splittings (Figure 3), the separation between the spin-orbit split levels decreases for the ^{4}F levels, but may increase modestly for the ^{4}I levels (Figure 9). A decreased electron density induced by enhanced covalency would be generally anticipated to decrease spin-orbit coupling, as is clearly the case for the ^{4}F level. We have no simple explanation for the enhanced spin-orbit coupling of the ^{4}I level. Lastly, the splittings of the Stark levels are expected to be enhanced by both increased distortion and enhanced crystal field strength (e.g., Tröster 2003). This is clearly observed over the pressure range of our experiments, with the spread between levels (the shaded regions in Figure 9) clearly expanding under pressure. Indeed, the maximum value of Stark splitting has been shown to scale with the crystal field strength at the site (Auzel and Malta 1983).

459 **Anomalous pressure shifts in Nd^{3+} luminescence**

460 Overall, the general expectation is that luminescence lines will shift to lower energy with
461 pressure; as pressure is increased, the ligands bound to the Nd^{3+} ion are brought closer to the
462 Nd^{3+} ion, and all electronic levels move to higher energy, but the overarching trend is that higher
463 lying levels tend to shift less quickly to higher energies than lower levels. Thus, the effect of the
464 change in spatial distance between the REE and ligands causes the energy difference between the
465 ground state and the excited states to become lessened with compaction. Previously, anomalous
466 behavior has been observed in the perovskite structured Nd^{3+} doped $YAlO_3$: blueshifts of a
467 subset of peaks associated with the transition from $^4F_{3/2}$ to $^4I_{9/2}$ have been observed (Barnett et al.
468 1973; Hua and Vohra 1997; Hernández-Rodríguez et al. 2018a). These anomalous shifts have
469 been attributed to a combination of increasing crystal field strength (and hence splitting) and
470 hybridization of the f-orbitals (Hernández-Rodríguez et al. 2018a). The vast majority of the
471 luminescence bands shift to lower energy with pressure in bastnäsite. However, two
472 luminescence bands have pressure shifts that involve an increase in energy in bastnäsite-II
473 ($^2H_{9/2}$→$^4I_{9/2}$, peak 23; and $^4F_{3/2}$->$^4I_{9/2}$, peak 3), and two increases in bastnäsite-III: the new mode
474 associated with R2 peak 1 and peak 6 in $^4F_{3/2}$→ $^4I_{9/2}$. Notably, these bands are among the higher
475 energy lines associated with each of their respective transitions; hence, the role of enhanced
476 Stark splitting counterbalances the general decrease in energy of the barycenter of their
477 respective transitions. Thus, these atypical shifts can be attributed to complex crystal field
478 interactions between the Nd^{3+} ion and O/F ligands induced by an enhanced site distortion, and
479 hence anisotropic compression within the REE site.

480 **Implications**

481 The bonding of both the carbonate units and neodymium ions under pressure is
482 constrained in this critically important ore mineral. Notably, bastnäsite undergoes two apparently
483 distortional phase transitions under compression: the first, near 25 GPa, appears to involve
484 primarily a shift in the symmetry of the carbonate ion, while the second, which initiates at 38
485 GPa, generates a second REE site in this material. From an overarching perspective, the overall
486 layered bonding of the bastnäsite structure, with REE-F layers and carbonate layers, appears
487 remarkably stable under compression: no indication is seen within this pressure range of any
488 weakening of C-O bonds that would indicate an incipient increase in coordination, or onset of
489 dimerization associated with the carbonate group (e.g., Vennari et al. 2018). The general
490 structural stability of this phase indicates that REE retention in the Earth's mantle may continue
491 to involve bonding within phases containing both halogens and carbonate ions. Hence, REE
492 element cycling, which has been used to constrain mantle differentiation, may critically depend
493 on the presence of trace carbonate- and/or halogen-bearing phases at depth. Thus, the affinity of
494 REE for carbonatite-associated lithologies in the near surface may persist to depth within the
495 planet.
496 From a high-pressure science perspective, bastnäsite (which is quite stable under
497 compression at 300 K) could represent a candidate for a high pressure luminescent calibrant in
498 the near IR region from 0 to ~38 GPa: the transition from R1 to Y2 (Band 14), which is an
499 intense mode in the NIR region does not split under pressure and shifts robustly and
500 continuously through the transition from bastnäsite-I and -II. Furthermore, the splitting between
501 two of the other intense peaks (R1 and R2) may provide a sensitive probe of the degree of
502 distortion of REE sites within a range of REE-bearing oxides and halides under compression.
503

Acknowledgments

We would especially like to thank Simon Teat for assistance with the single crystal X-ray diffraction. We would also like to thank Christine Beavers, Myriam Telus, Laura McCormick, Nico Giordano, Earl O'Bannon and Ben Dejarnatt for discussions and assistance with the sample analyses. We thank three anonymous reviewers for comments that substantially improved the manuscript, and would like to thank Andrew Doran for help with gas-loading. This work was supported by the US NSF (EAR-1620423) and with partial support from COMPRES under the National Science Foundation Cooperative Agreement (EAR-1606856). This research used resources of the Advanced Light Source (beamline 12.2.1) at Lawrence Berkeley National Laboratory which is DOE Office of Science User facility under Contract No. DE-AC02-05CH11231.

References

Auzel, F., and Malta, O.L. (1983) A scalar crystal field strength parameter for rare-earth ions: Meaning and usefulness. Journal de Physique, 44, 201–206.

Barnett, J.D., Block, S., and Piermarini, G.J. (1973) An optical fluorescence system for quantitative pressure measurement in the diamond-anvil cell. Review of Scientific Instruments, 44, 1–9.

Bray, K.L. (2001) High pressure probes of electronic structure and luminescence properties. In H. Yersin, Ed., Transition Metal and Rare Earth Compounds: Excited States, Transitions, Interactions, I pp. 1–94. Springer-Verlag Berlin Heidelberg, New York.

Brenker, F.E., Vollmer, C., Vincze, L., Vekemans, B., Szymanski, A., Janssens, K., Szaloki, I., Nasdala, L., Joswig, W., and Kaminsky, F. (2007) Carbonates from the lower part of transition zone or even the lower mantle. Earth and Planetary Science Letters, 260, 1–9.

Bruker (2013) SAINT V8.34A. Bruker AXS Inc., Madison, Wisconsin, USA.

——— (2016a) APEX3. Bruker AXS Inc., Madison, Wisconsin, USA.

——— (2016b) SADABS. Bruker AXS Inc., Madison, Wisconsin, USA.

Collerson, K.D., Williams, Q., Ewart, A.E., and Murphy, D.T. (2010) Origin of HIMU and EM-1 domains sampled by ocean island basalts, kimberlites and carbonatites: The role of CO_2-fluxed lower mantle melting in thermochemical upwellings. Physics of the Earth and Planetary Interiors, 181, 112–131.

DePaolo, D.J., and Wasserburg, G.J. (1976) Nd isotopic variations and petrogenic models. Geophysical Research Letters, 3, 249–252.

Dewaele, A., Torrent, M., Loubeyre, P., and Mezouar, M. (2008) Compression curves of transition metals in the Mbar range: Experiments and projector augmented-wave calculations. Physical Review B, 78, 1–13.

Dieke, G.H. (1969) Spectra and Energy Levels of Rare-Earth Ions in Crystals. Interscience, New York.

Dolan, J.F., Kappers, L.A., and Bartram, R.H. (1986) Pressure and temperature dependence of chromium photoluminescence in $K_2NaGaF_6:Cr^{3+}$. Physical Review B, 33, 7339–7341.

Donnay, G., and Donnay, J.D.H. (1953) The crystallography of bastnaesite, parisite, roentgenite, and synchisite. The American Mineralogist, 38, 932–963.

Freire, P.T.C., Pilla, O., and Lemos, V. (1994) Pressure-induced level crossing in $KZnF_3:Cr^{3+}$. Physical Review B, 49, 9232–9235.

Frost, R.L., and Dickfos, M.J. (2007) Raman spectroscopy of halogen-containing carbonates. Journal of Raman Spectroscopy, 38, 1516–1522.

Grice, J.D., Maisonneuve, V., and Leblanc, M. (2007) Natural and synthetic fluoride carbonates.

Chemical Reviews, 107, 114–132.

Henderson, J.R., Muramoto, M., and Gruber, J.B. (1967) Spectrum of Nd3+ in lanthanide oxide crystals. Journal of Chemical Physics, 46, 2515–2520.

Hernández-Rodríguez, M.A., Muñoz-Santiuste, J.E., Lavín, V., Lozano-Gorrín, A.D., Muñoz, A., Venkatramu, V., Martín, I.R., and Rodríguez-Mendoza, U.R. (2018a) High pressure luminescence of Nd3+ in YAlO3 perovskite nanocrystals: A crystal-field analysis. Journal of Chemical Physics, 148, 044201.

Hernández-Rodríguez, M.A., Rodríguez-Mendoza, U.R., Lavín, V., Muñoz-Santiuste, J.E., Martín, I.R., and Lozano-Gorrín, A.D. (2018b) High pressure sensitivity of anti-Stokes fluorescence in Nd^{3+} doped yttrium orthoaluminate nano-perovskites. Journal of Luminescence, 196, 20–24.

Holtstam, D., and Andersson, U.B. (2007) The REE minerals of the Bastnas-type deposits, south-central Sweden. The Canadian Mineralogist, 45, 1073–1114.

Hua, H., and Vohra, Y.K. (1997) Pressure-induced blueshift of Nd^{3+} fluorescence emission in $YAlO_3$: Near infrared pressure sensor. Applied Physics Letters, 71, 2602–2604.

Hua, H., Mirov, S., and Vohra, Y. (1996) High-pressure and high-temperature studies on oxide garnets. Physical Review B, 54, 6200–6209.

Hübschle, C.B., Sheldrick, G.M., and Dittrich, B. (2011) ShelXle: A Qt graphical user interface for SHELXL. Journal of Applied Crystallography, 44, 1281–1284.

Jago, B.C., and Gittins, J. (1991) The role of fluorine in carbonatite magma evolution. Nature, 349, 56–58.

Jones, A.P., Genge, M., and Carmody, L. (2013) Carbonate Melts and Carbonatites. Reviews in Mineralogy and Geochemistry, 75, 289–322.

573 Kaminskii, A.A. (1981) Laser Crystals Their Physics and Properties, 1st ed. Springer-Verlag
574 Berlin Heidelberg, New York.
575 Klotz, S., Chervin, J.-C., Munsch, P., and Le Marchand, G. (2009) Hydrostatic limits of 11
576 pressure transmitting media. Journal of Physics D: Applied Physics, 42, 075413.
577 Kraft, S., Knittle, E., and Williams, Q. (1991) Carbonate stability in the Earth's mantle: A
578 vibrational spectroscopic study of aragonite and dolomite at high pressures and
579 temperatures. Journal of Geophysical Research, 96, 17997–18009.
580 Lenz, C., Talla, D., Ruschel, K., Škoda, R., Götze, J., and Nasdala, L. (2013) Factors affecting
581 the Nd^{3+} (REE^{3+}) luminescence of minerals. Mineralogy and Petrology, 107, 415–428.
582 Mao, H.K., Xu, J., and Bell, P.M. (1986) Calibration of the ruby pressure gauge to 800 kbar
583 under quasi-hydrostatic conditions. Journal of Geophysical Research, 91, 4673–4676.
584 McCulloch, M.T., and Wasserburg, G.T. (1978) Sm-Nd and Rb-Sr chronology of continental
585 crust formation. Science, 200, 1003–1011.
586 Muñoz Santiuste, J.E., Lavín, V., Rodríguez-Mendoza, U.R., Tardio, M.M., and Ramírez-
587 Jiménez, R. (2017) Pressure-induced effects on the spectroscopic properties of Nd^{3+} in
588 MgO:$LiNbO_3$ single crystal. A crystal field approach. Journal of Luminescence, 184, 293–
589 303.
590 Ni, Y., Hughes, J.M., and Mariano, A.N. (1993) The atomic arrangement of bastnasite-(Ce),
591 $Ce(CO_3)F$, and structural elements of synchysite-(Ce), rontgenite-(Ce), and parisite-(Ce).
592 American Mineralogist, 78, 415–418.
593 O'Bannon, E., and Williams, Q. (2016) A Cr3+luminescence study of spodumene at high
594 pressures: Effects of site geometry, a phase transition, and a level-crossing. American
595 Mineralogist, 101, 1406–1413.

Pokhrel, M., Ray, N., Kumar, G.A., and Sardar, D.K. (2012) Comparative studies of the spectroscopic properties of Nd^{3+}: YAG nanocrystals, transparent ceramic and single crystal. Optical Materials Express, 2, 235.

Rowland II, R.L. (2017) Phase Equilibria, Compressibility, and Thermal Analysis of Bastnaesite-(La). M.S. Thesis, University of Nevada Las Vegas.

Sardar, D.K., and Yow, R.M. (1998) Optical characterization of inter-Stark energy levels and effects of temperature on sharp emission lines of Nd^{3+} in $CaZn_2Y_2Ge_3O_{12}$. Optical Materials, 10, 191–199.

Sharp, E.J., Miller, J.E., Horowitz, D.J., Linz, A., and Belruss, V. (1974) Optical spectra and laser action in Nd^{3+}-doped $CaY_2Mg_2Ge_3O_{12}$. Journal of Applied Physics, 45, 4974–4979.

Sheldrick, G.M. (2015) SHELXT - Integrated space-group and crystal-structure determination. Acta Crystallographica Section A, 71, 3–8.

Tröster, T. (2003) Optical studies of non-metallic compounds under pressure. In J. K. A. Gschneidner, J.-C.G. Bunzli, and V.K. Pecharsky, Eds., Handbook on the Physics and Chemistry of Rare Earths Vol. 33, pp. 515–589. Elsevier Science B.V.

Turner, D., Rivard, B., and Groat, L. (2015) Visible to shortwave infrared reflectance spectroscopy of rare earth element minerals. Symposium on Strategic and Critical Materials Proceedings, 219–229.

Vennari, C.E., and Williams, Q. (2018) A novel carbon bonding environment in deep mantle high-pressure dolomite. American Mineralogist, 103, 171–174.

Vennari, C.E., Beavers, C.M., and Williams, Q. (2018) High-Pressure/Temperature Behavior of the Alkali/Calcium Carbonate Shortite ($Na_2Ca_2(CO_3)_3$): Implications for Carbon Sequestration in Earth's Transition Zone. Journal of Geophysical Research: Solid Earth,

123.

Williams, Q., and Knittle, E. (2003) Structural complexity in carbonatite liquid at high pressures. Geophysical Research Letters, 30, 30–33.

This is a preprint, the final version is subject to change, of the American Mineralogist (MSA)
Cite as Authors (Year) Title. American Mineralogist, in press.
DOI: https://doi.org/10.2138/am-2019-7011

Tables

Table 1. Raman modes as a function of pressure and calculated mode Grüneisen parameters of bastnäsite-I up to 25 GPa. *Bulk modulus of 105 GPa used from the La/F bastnäsite endmember (Rowland 2017).

ν_0 (cm^{-1})	Assignment	$d\nu/dP$ (cm^{-1}/GPa)	Grüneisen parameter*
112	Lattice mode	0.59(9)	0.53
129	Lattice mode	1.95(4)	1.59
162	Lattice mode	2.53(16)	1.64
188	Lattice mode	2.74(14)	1.54
238	Lattice mode	3.63(28)	1.60
258	Lattice mode	4.19(16)	1.70
272	Lattice mode	4.36(18)	1.68
303	Lattice mode	4.33(14)	1.50
350	Lattice mode	3.90 (24)	1.17
396	Lattice mode	4.35(14)	1.15
-	$(CO_3)^{2-}$ in-plane bend (ν_{4a})	0.89(10)	-
684	$(CO_3)^{2-}$ in-plane bend (ν_{4b})	1.28(6)	0.20
726	$(CO_3)^{2-}$ in-plane bend (ν_{4c})	1.51(8)	0.22
734	$(CO_3)^{2-}$ in-plane bend (ν_{4d})	1.60(6)	0.23
864	$(CO_3)^{2-}$ out-of-plane bend (ν_2)	-	-
868	$(CO_3)^{2-}$ out-of-plane bend (ν_2)	-0.29(8)	-0.04
1094	$(CO_3)^{2-}$ symmetric stretch (ν_1)	2.79(13)	0.30
1434	$(CO_3)^{2-}$ asymmetric stretch (ν_3)	-	-

This is a preprint, the final version is subject to change, of the American Mineralogist (MSA)
Cite as Authors (Year) Title. American Mineralogist, in press.
DOI: https://doi.org/10.2138/am-2019-7011

630 Table 2. Raman modes as a function of pressure of bastnäsite-II from 25 to 38 GPa. *ν_0 is at 25

631 GPa.

ν_0 (cm^{-1})*	Assignment	$d\nu/dP$ (cm^{-1}/GPa)
128	Lattice mode	0.52(3)
175	Lattice mode	1.66(4)
228	Lattice mode	1.77(6)
284	Lattice mode	1.76(8)
322	Lattice mode	2.20(11)
362	Lattice mode	2.61(9)
403	Lattice mode	2.92(11)
436	Lattice mode	2.82(9)
444	Lattice mode	2.88(8)
473	Lattice mode	3.35(15)
488	Lattice mode	2.92(8)
506	Lattice mode	3.06(1)
687	$(CO_3)^{2-}$ in-plane bend (ν_{4a})	0.87(6)
717	$(CO_3)^{2-}$ in-plane bend (ν_{4b})	0.98(2)
765	$(CO_3)^{2-}$ in-plane bend (ν_{4c})	1.39(3)
775	$(CO_3)^{2-}$ in-plane bend (ν_{4d})	1.09(7)
858	$(CO_3)^{2-}$ out-of-plane bend (ν_2)	-0.49(2)
1158	$(CO_3)^{2-}$ symmetric stretch (ν_{1a})	1.66(7)
1164	$(CO_3)^{2-}$ symmetric stretch (ν_1)	2.09(7)

632

This is a preprint, the final version is subject to change, of the American Mineralogist (MSA)
Cite as Authors (Year) Title. American Mineralogist, in press.
DOI: https://doi.org/10.2138/am-2019-7011

633 Table 3. Raman modes as a function of pressure of bastnäsite-III from 38 to 50 GPa. *ν_0 is at 38

634 GPa.

ν_0 (cm^{-1})*	Assignment	$d\nu/dP$ (cm^{-1}/GPa)
119	Lattice mode	0.007(116)
127	Lattice mode	0.32(8)
139	Lattice mode	0.40(4)
203	Lattice mode	1.39(8)
258	Lattice mode	1.59(5)
271	Lattice mode	1.84(12)
367	Lattice mode	2.50(17)
404	Lattice mode	1.74(4)
425	Lattice mode	2.75(17)
488	Lattice mode	2.07(29)
537	Lattice mode	2.65(6)
558	Lattice mode	2.43(5)
703	$(CO_3)^{2-}$ in-plane bend (ν_{4a})	0.78(4)
733	$(CO_3)^{2-}$ in-plane bend (ν_{4b})	0.85(4)
794	$(CO_3)^{2-}$ in-plane bend (ν_{4d})	1.23(5)
848	$(CO_3)^{2-}$ out-of-plane bend (ν_{2a})	-0.68(9)
852	$(CO_3)^{2-}$ out-of-plane bend (ν_2)	-0.31(4)
864	$(CO_3)^{2-}$ out-of-plane bend (ν_{2b})	-0.007(162)
1186	$(CO_3)^{2-}$ symmetric stretch (ν_{1a})	1.54(5)
1192	$(CO_3)^{2-}$ symmetric stretch (ν_{1b})	1.79(8)
1197	$(CO_3)^{2-}$ symmetric stretch (ν_1)	1.81(7)

635

This is a preprint, the final version is subject to change, of the American Mineralogist (MSA)
Cite as Authors (Year) Title. American Mineralogist, in press.
DOI: https://doi.org/10.2138/am-2019-7011

636 Table 4. $^4F3_{/2}$->$^4I_{9/2}$ luminescence as a function of pressure in bastnäsite.

Assignment	λ_0 (nm)	ν_0 (cm^{-1})	Bastnäsite-I to 25 GPa (cm^{-1}/GPa)	Bastnäsite-II 25 to 40 GPa (cm^{-1}/GPa)	Bastnäsite-II 40 to 50 GPa (cm^{-1}/GPa)
1*					1.05(33)
1	862.91	11,588.7	0.42(2)	-0.27(11)	-0.12(7)
2	864.96	11,561.2	0.20(9)	-0.31(16)	-0.83(11)
3	868.47	11,514.5	-1.84(24)	1.43(48)	-1.13(13)
4	870.63	11,485.9	-1.67(10)	-0.48(2)	-0.87(29)
4*					-1.76(37)
5	874.51	11,435.0	-3.51(26)	-1.14(94)	-1.37(88)
6	876.80	11,405.1	-3.35(13)	-1.61(15)	0.16(62)
7*					-2.76(36)
7	887.95	11,261.9	-5.99(23)	-3.57(14)	-4.28(7)
8	889.68	11,240.0	-6.40(26)	-4.63(15)	-4.08(24)
9	897.84	11,137.8	-6.73(19)	-5.26(10)	-5.62(25)
10	900.23	11,108.3	-6.95(8)	-4.93(40)	-4.75(134)
10*					-5.16(2)

637
638

This is a preprint, the final version is subject to change, of the American Mineralogist (MSA)
Cite as Authors (Year) Title. American Mineralogist, in press.
DOI: https://doi.org/10.2138/am-2019-7011

639 Table 5. $^4F_{3/2} \rightarrow {}^4I_{11/2}$ luminescence as a function of pressure in bastnäsite.

Assignment	λ_0 (nm)	ν_0 (cm^{-1})	Bastnäsite-I to 25 GPa (cm^{-1}/GPa)	Bastnäsite-II 25 to 40 GPa (cm^{-1}/GPa)	Bastnäsite-II 40 to 50 GPa (cm^{-1}/GPa)
11	1046.83	9,552.7	-1.91(11)	-1.26(40)	-2.35(51)
12	1049.86	9,525.1	-2.21(4)	-1.59(5)	-2.19(10)
13*			-2.47(12)	-2.99(14)	-2.33(22)
13	1051.0	9,514.7	-4.00(27)		
14	1054.01	9,487.6	-4.42(14)	-3.08(13)	-2.78(33)
14*					-3.54(50)
15	1056.82	9,462.3	-4.77(7)	-4.57(27)	-5.84(37
16	1060.09	9,433.2	-4.91(13)		
17	1062.86	9,408.6	-5.26(4)	-6.00(39)	-5.35(86)
18	1065.77	9,382.9	-6.35(27)		

640
641

This is a preprint, the final version is subject to change, of the American Mineralogist (MSA)
Cite as Authors (Year) Title. American Mineralogist, in press.
DOI: https://doi.org/10.2138/am-2019-7011

642 Table 6. $^4F_{5/2}+^2H_{9/2}\rightarrow{}^4I_{9/2}$ luminescence as a function of pressure in bastnäsite.

Assignment	λ_0 (nm)	ν_0 (cm^{-1})	Bastnäsite-I to 25 GPa (cm^{-1}/GPa)	Bastnäsite-II 25 to 40 GPa (cm^{-1}/GPa)	Bastnäsite-II 40 to 50 GPa (cm^{-1}/GPa)
23 ($^2H_{9/2}$)	791.46	12,634.9	-0.37(8)	0.57(9)	-0.49(18)
24 ($^2H_{9/2}$)			-0.04(7)	-0.73(7)	-1.30(13)
24*($^2H_{9/2}$)			-1.52(33)	-2.01(12)	-1.90(21)
25* ($^2H_{9/2}$)					-2.00(24)
25 ($^2H_{9/2}$)	793.65	12,600.0	-1.94(6)	-2.51(11)	
26a ($^2H_{9/2}$)			-2.30(25)	-0.80(19)	-0.60(23)
26a*($^2H_{9/2}$)				-1.83(15)	-2.04(33)
26a**					-2.00(37)
26* ($^2H_{9/2}$)				-3.72(29)	-0.73(70)
26 ($^2H_{9/2}$)	798.04	12,530.7	-5.05(47)	-3.20(11)	-3.08(75)
27 ($^2H_{9/2}$)	803.34	12,448.0	-3.82(18)	-3.19(37)	2.79(28)
28 ($^4F_{5/2}$)	807.94	12,377.2	-4.41(68)	-3.93(54)	-3.16(76)
29 ($^4F_{5/2}$)	814.90	12,271.4	-5.98(32)	-4.36(21)	-0.93(43)
30 ($^4F_{5/2}$)	822.71	12,155.0	-7.22(14)	-4.99(22)	

643

644

Figure Captions

Figure 1. The ambient crystal structure of bastnäsite with the unit cell delineated by black lines; as per the labels, dark green spheres are fluorine, lime green is the REE, black is carbon, and red is oxygen.

Figure 2. Ambient pressure and temperature (a) Raman spectrum and (b) luminescence spectrum of bastnäsite; black is the measured spectrum, gray are the deconvolved peaks, red is the calculated intensities, and blue is the background. The relative intensities for the $^4F_{5/2}+^2H_{5/2}\rightarrow{}^4I_{9/2}$ are increased by 3x, and the $4F_{3/2}\rightarrow{}^4I_{9/2}$ section was collected for 6x longer than the other two luminescence regions.

Figure 3. (left) Schematic representation of the f-electron energy levels of Nd^{3+} in bastnäsite showing the effects of Coulombic repulsion, spin-orbit coupling, and crystal-field interactions. (right) Partial energy level diagram of Nd^{3+} in bastnäsite showing the major spin-orbit coupling induced energy levels.

Figure 4. (a and b) Representative Raman spectra of the lattice and carbonate spectral regions under compression, arrows indicate new peaks in Raman spectrum; (c) deconvolution of the symmetric stretch of the Raman spectrum of bastnäsite at 50.6 GPa, the highest pressure probed; (d and e) peak positions of observed Raman modes as a function of pressure at room temperature under compression.

Figure 5. (a) Luminescence spectra of the $^4F_{3/2}\rightarrow{}^4I_{9/2}$ transition in Nd^{3+} as a function of pressure. Partial energy level diagram is shown on the right. (b) Peak positions of observed luminescence modes with pressure.

Figure 6. (a) Luminescence spectra of the $^4F_{3/2} \rightarrow {}^4I_{11/2}$ transition in Nd^{3+} as a function of pressure. Luminescence spectra are produced by 633 nm excitation. (b) Peak positions of the observed luminescence bands with pressure.

Figure 7. Luminescence spectra of the $^4F_{5/2}+{}^2H_{9/2} \rightarrow {}^4I_{9/2}$ transition in Nd^{3+} as a function of pressure. Luminescence spectra are produced by 633 nm excitation. (b) Peak positions of observed luminescence bands with pressure.

Figure 8. R-line separation of Nd^{3+} (R_1 and R_2) in the original REE site(closed circles), and associated with the new high-pressure site in bastnäsite-III (closed triangles), as a function of pressure.

Figure 9. Energy levels of Nd^{3+} with pressure; shaded regions designate the observed spread in energy levels, and lines represent the barycenters of the Stark levels, with the exception of the $^4I_{9/2}$ level, where the line represents the ground state of the system.

This is a preprint, the final version is subject to change, of the American Mineralogist (MSA)
Cite as Authors (Year) Title. American Mineralogist, in press.
DOI: https://doi.org/10.2138/am-2019-7011

Figure 1

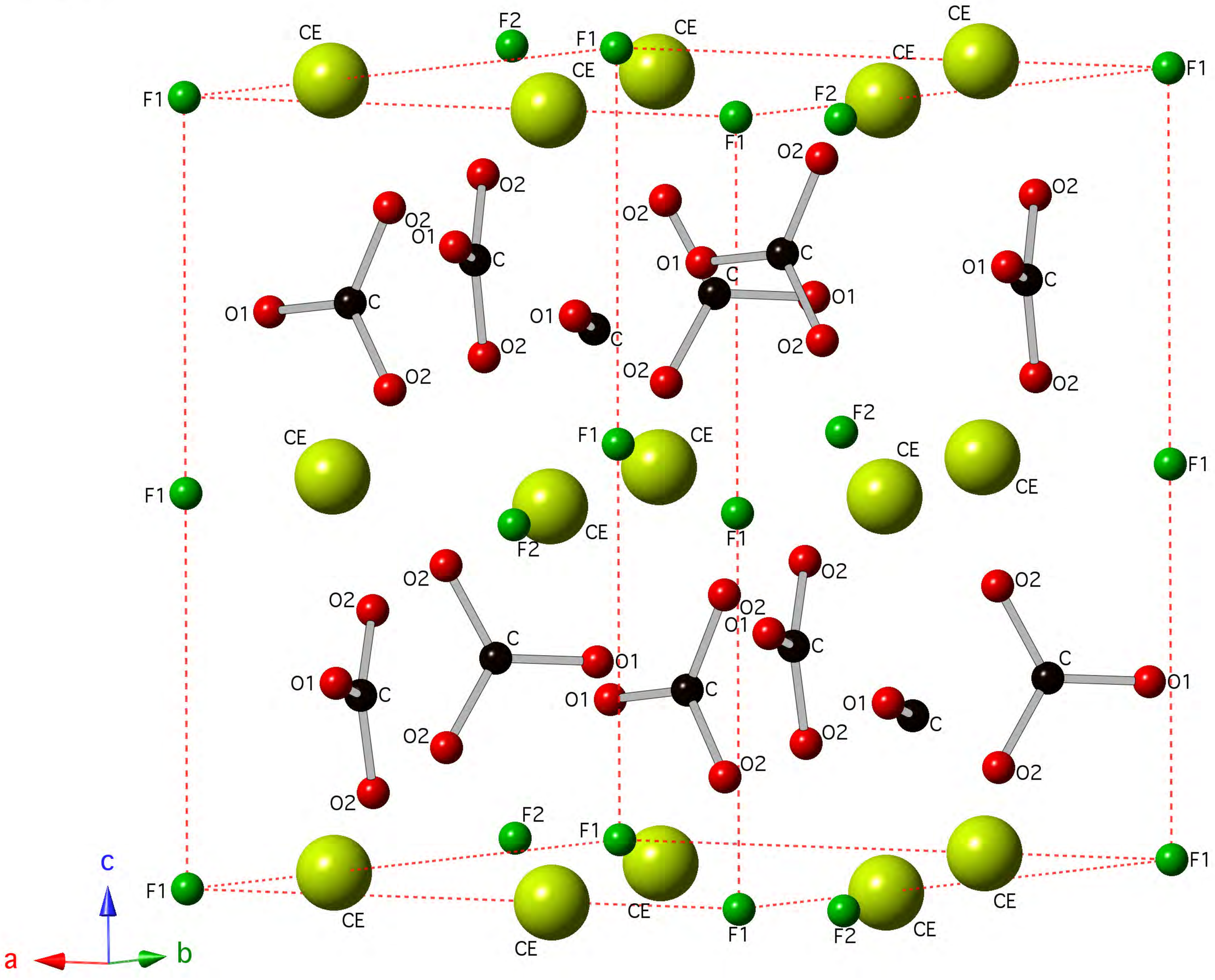

Figure 2a

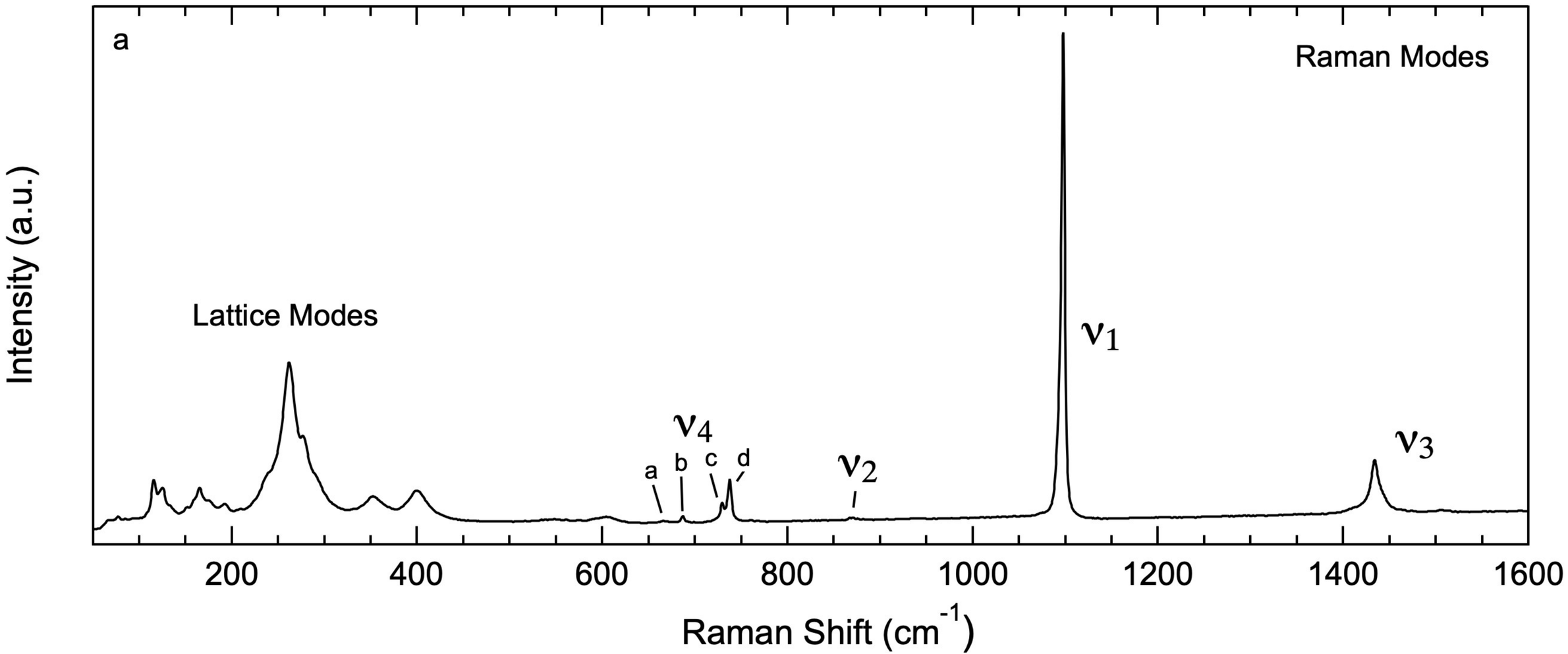

Figure 2b

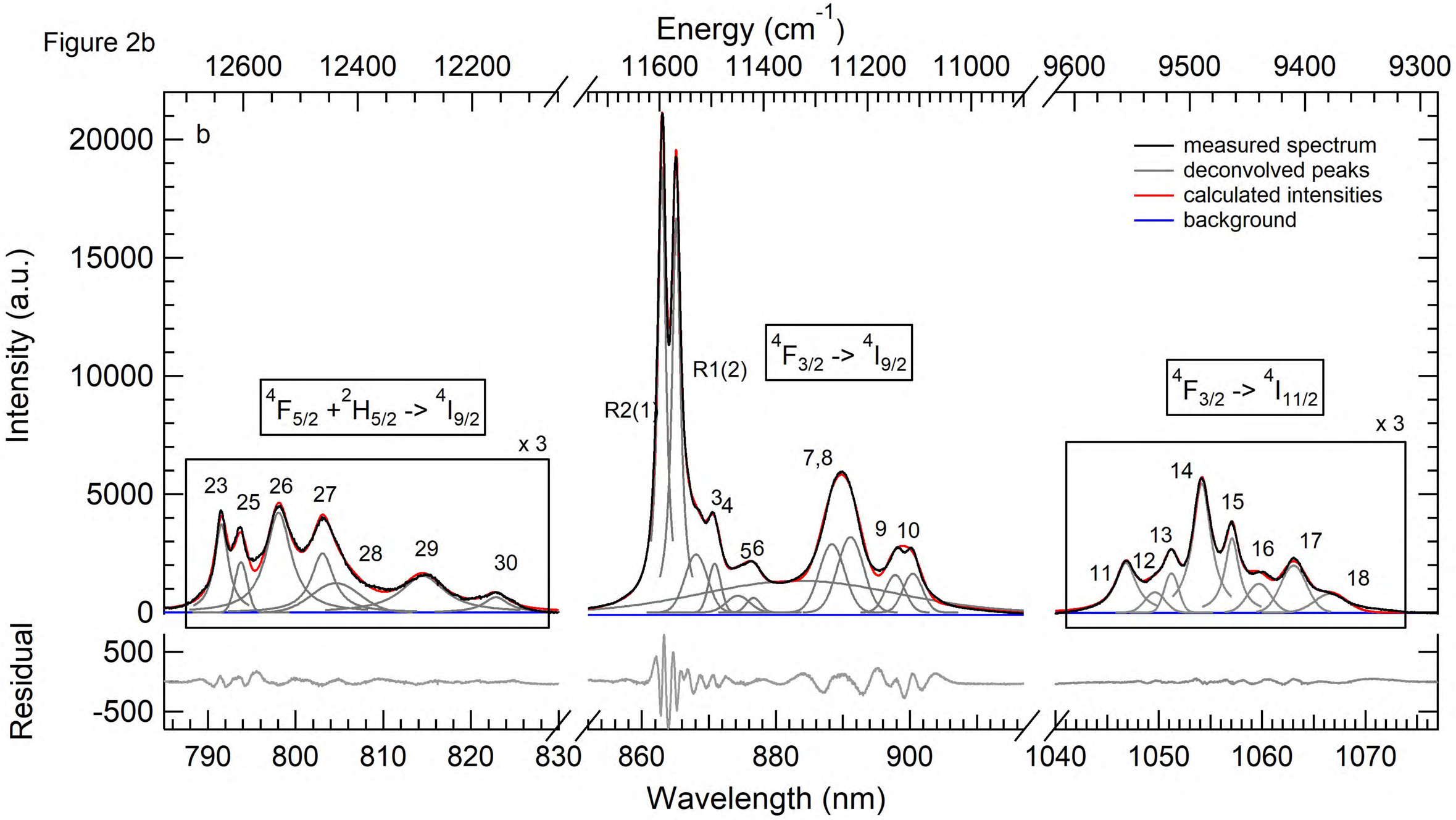

This is a preprint, the final version is subject to change, of the American Mineralogist (MSA)
Cite as Authors (Year) Title. American Mineralogist, in press.
DOI: https://doi.org/10.2138/am-2019-7011

Figure 3

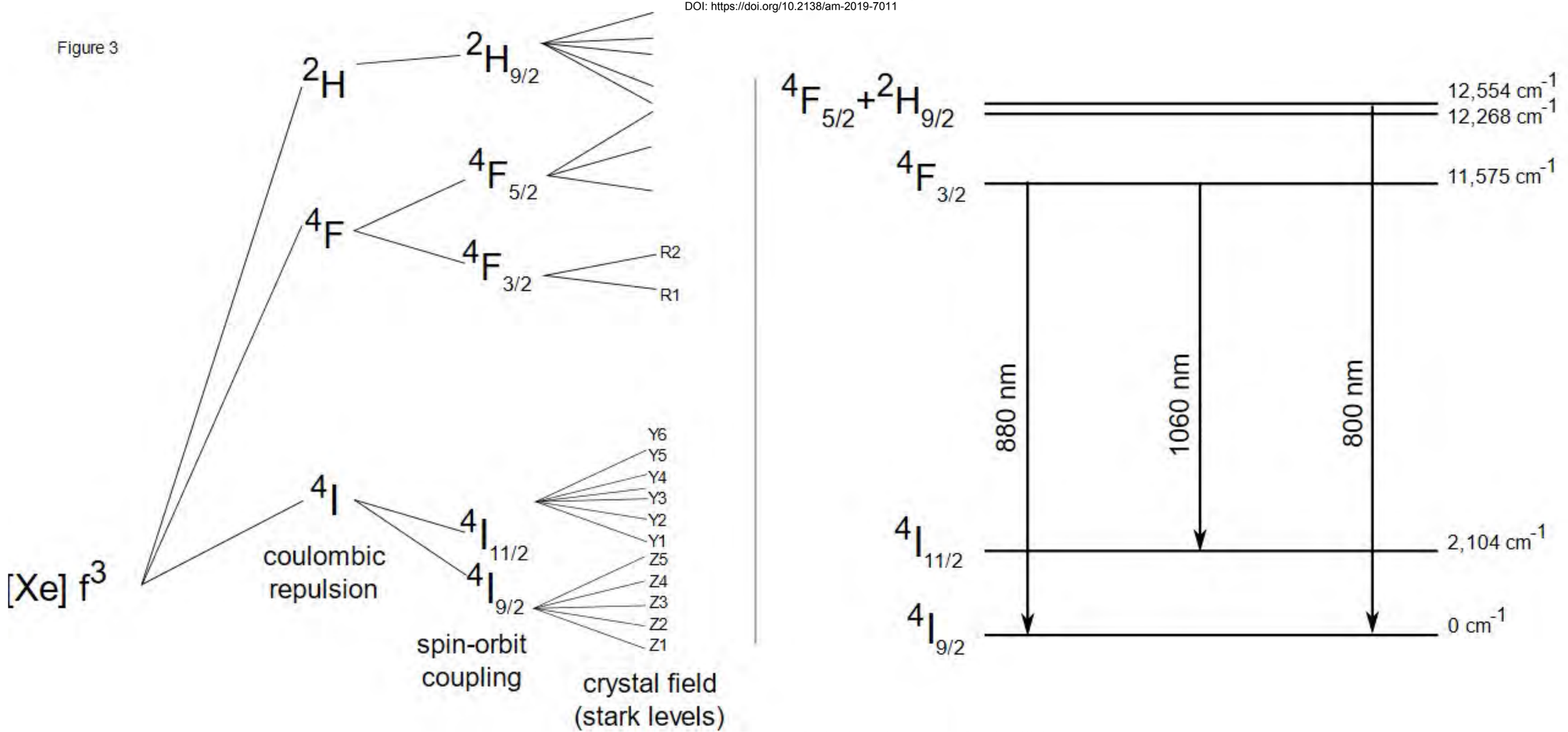

This is a preprint, the final version is subject to change, of the American Mineralogist (MSA)
Cite as Authors (Year) Title. American Mineralogist, in press.
DOI: https://doi.org/10.2138/am-2019-7011

Figure 4a

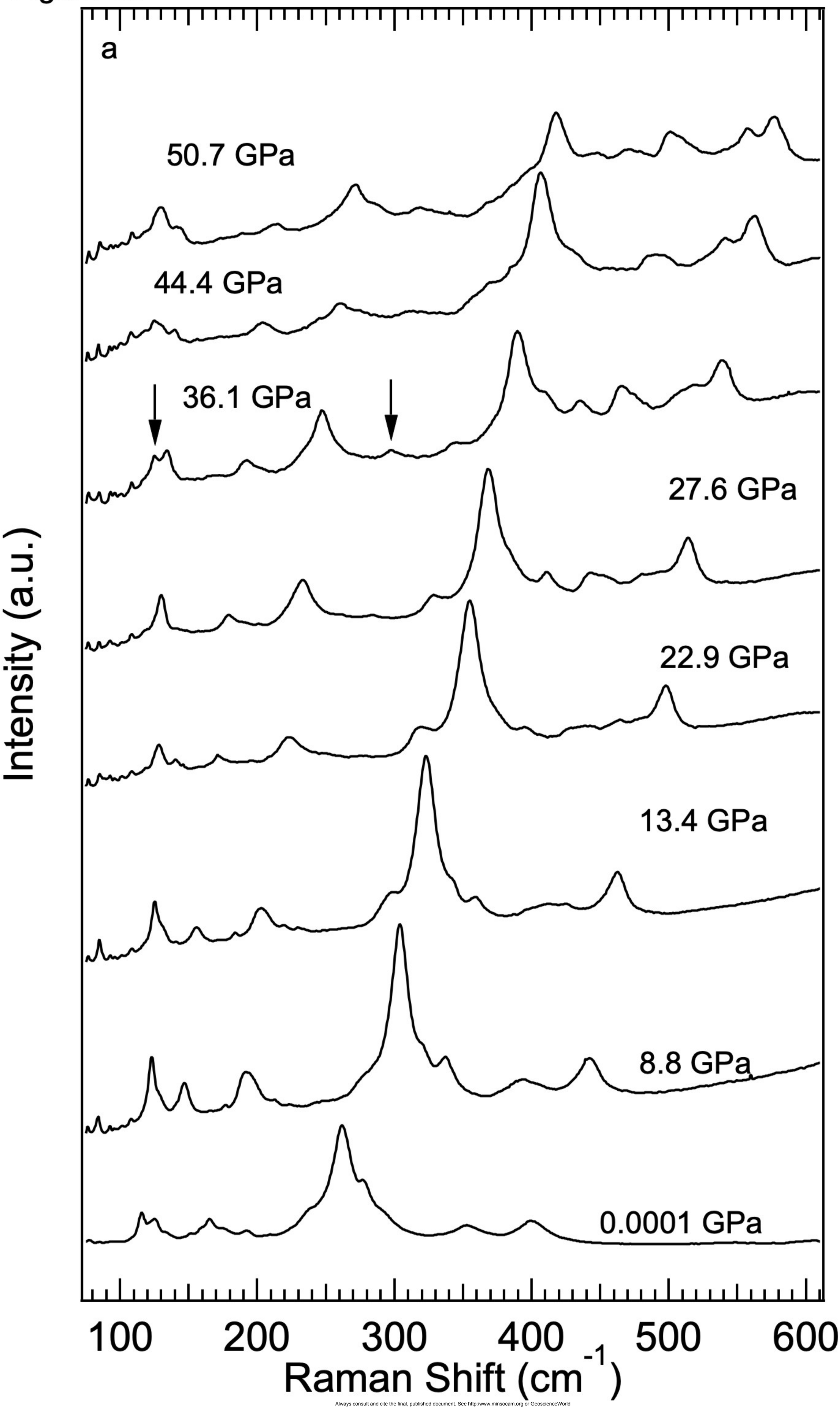

Figure 4b

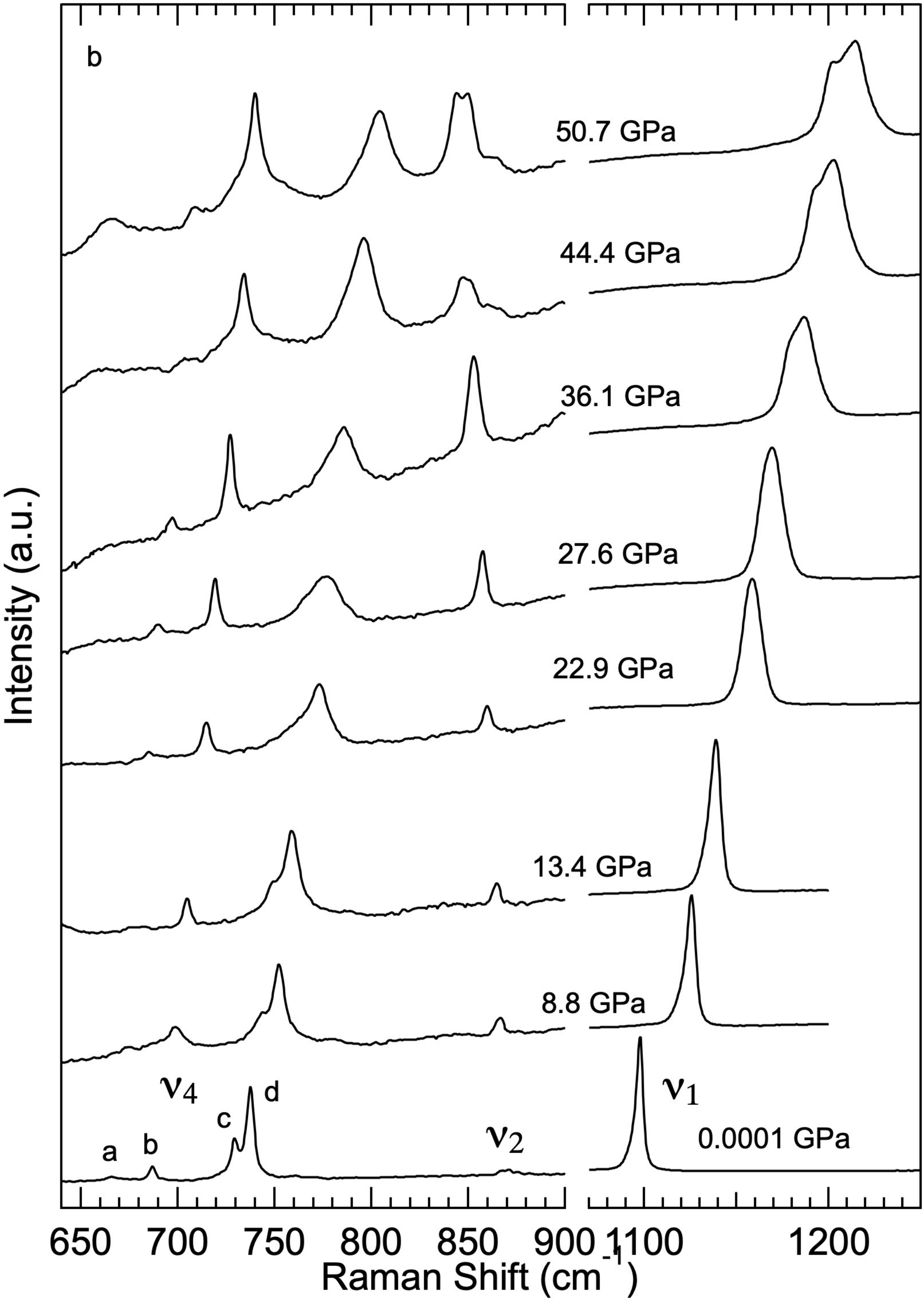

This is a preprint, the final version is subject to change, of the American Mineralogist (MSA)
Cite as Authors (Year) Title. American Mineralogist, in press.
DOI: https://doi.org/10.2138/am-2019-7011

Figure 4c

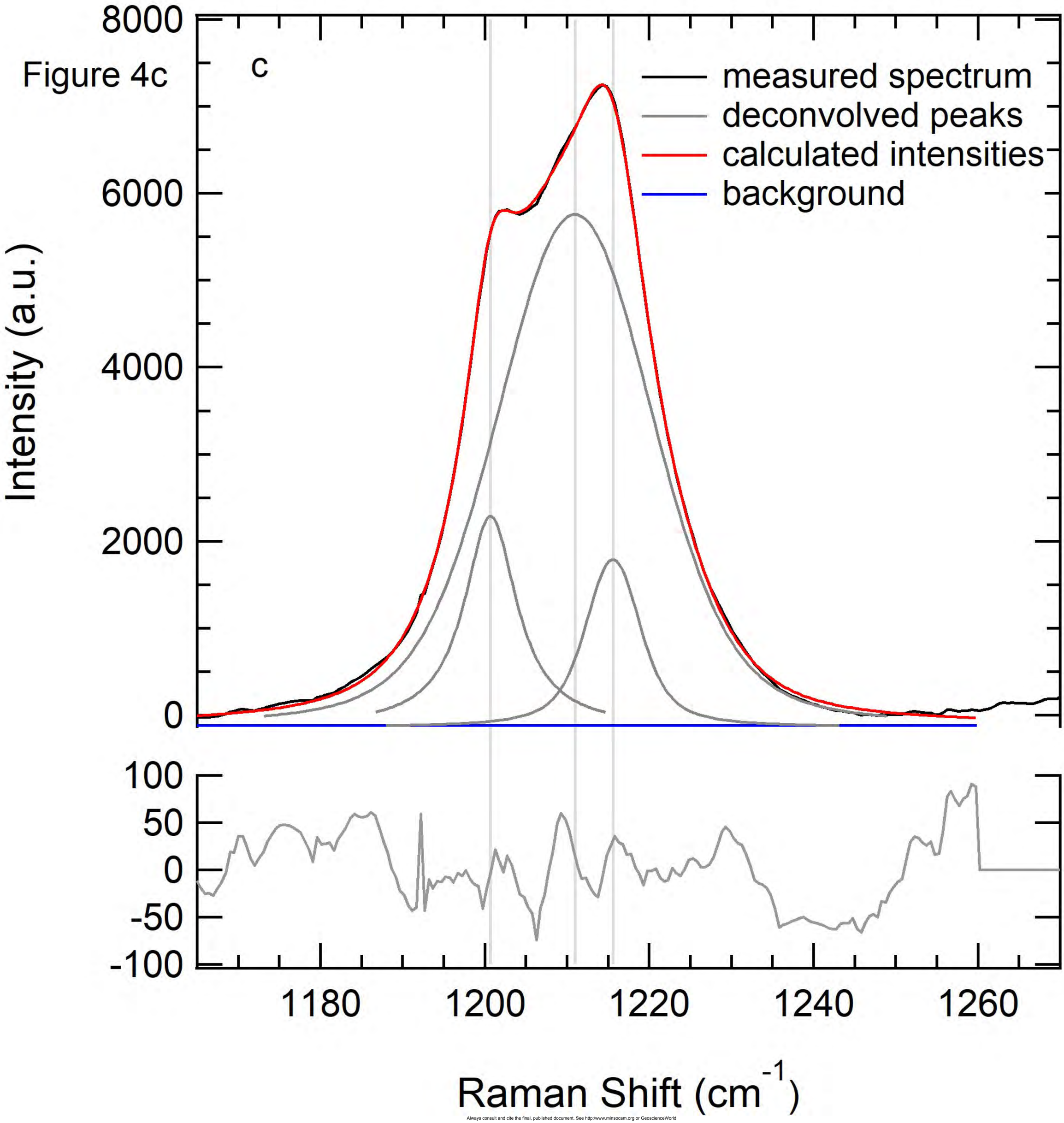

This is a preprint, the final version is subject to change, of the American Mineralogist (MSA)
Cite as Authors (Year) Title. American Mineralogist, in press.
DOI: https://doi.org/10.2138/am-2019-7011

Figure 4d

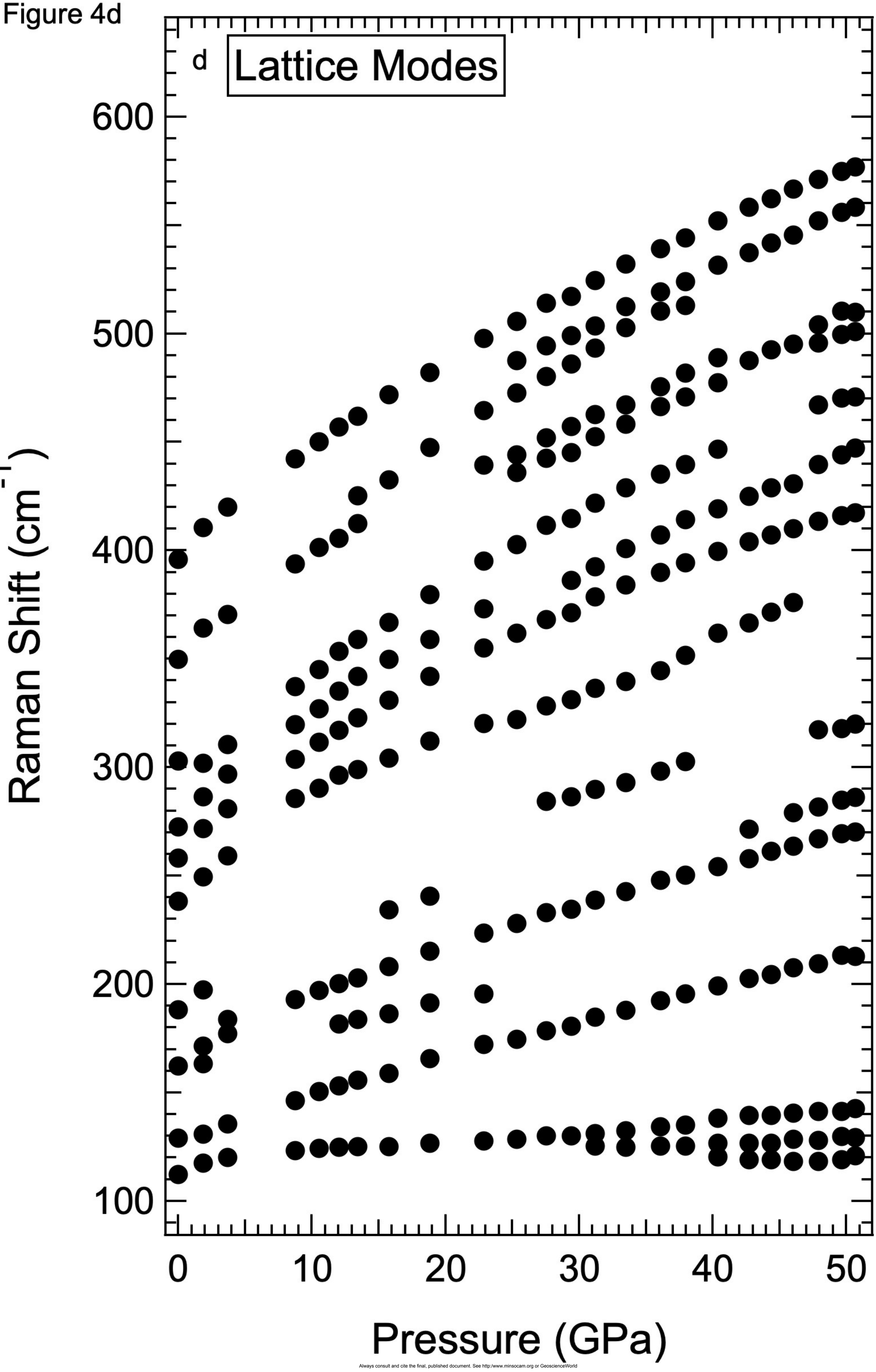

This is a preprint, the final version is subject to change, of the American Mineralogist (MSA)
Cite as Authors (Year) Title. American Mineralogist, in press.
DOI: https://doi.org/10.2138/am-2019-7011

Figure 4e

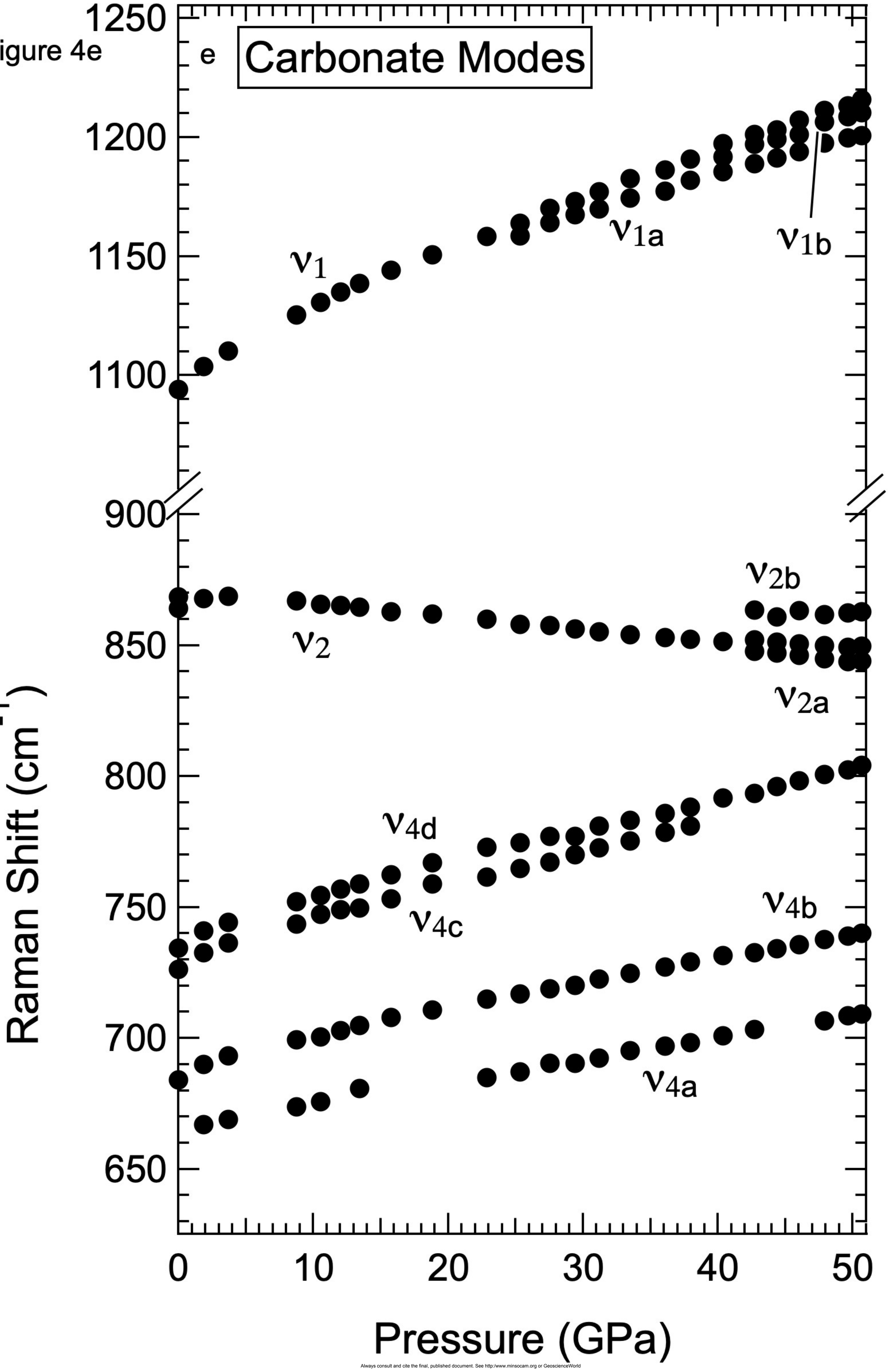

Figure 5ab

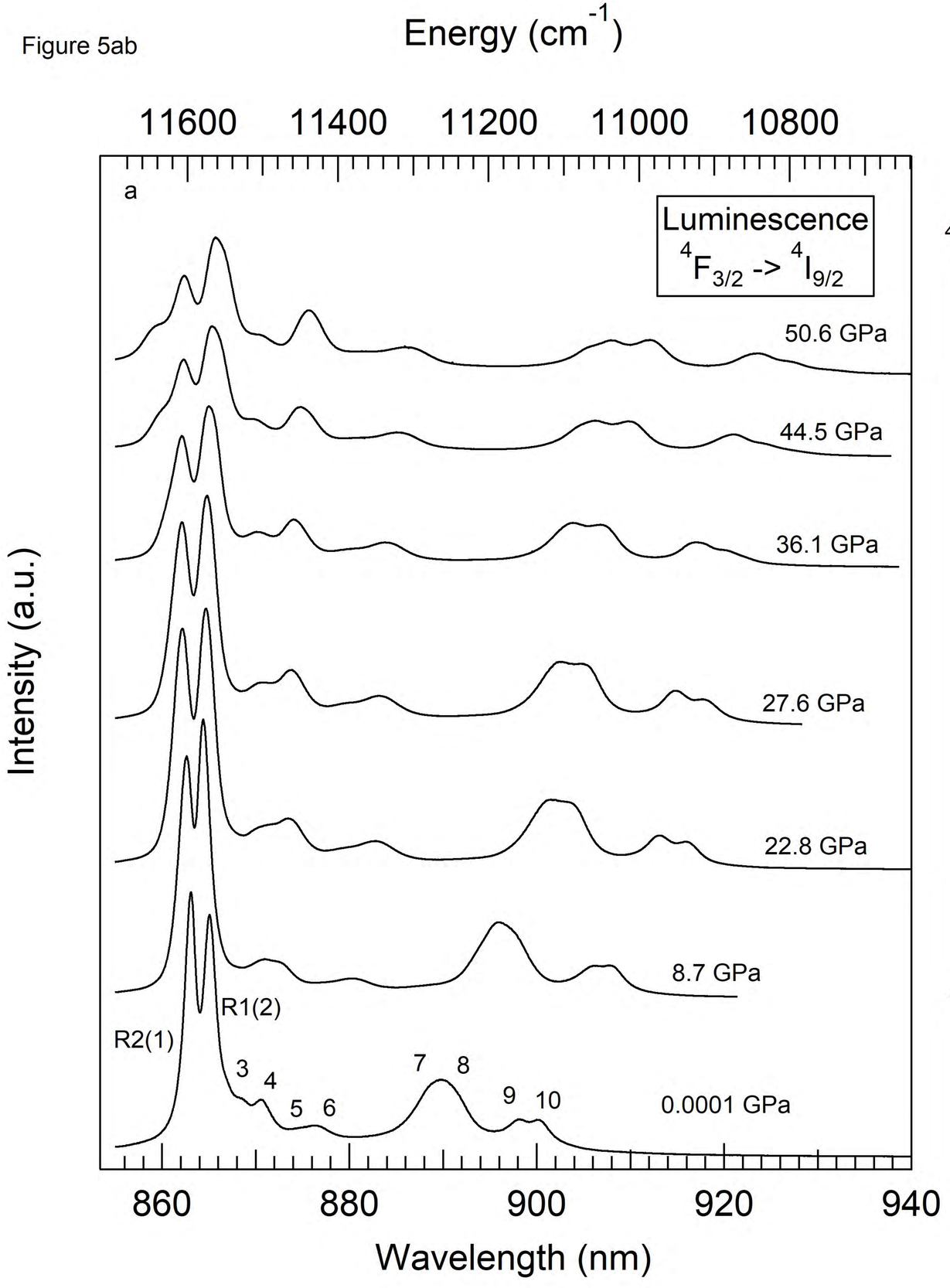

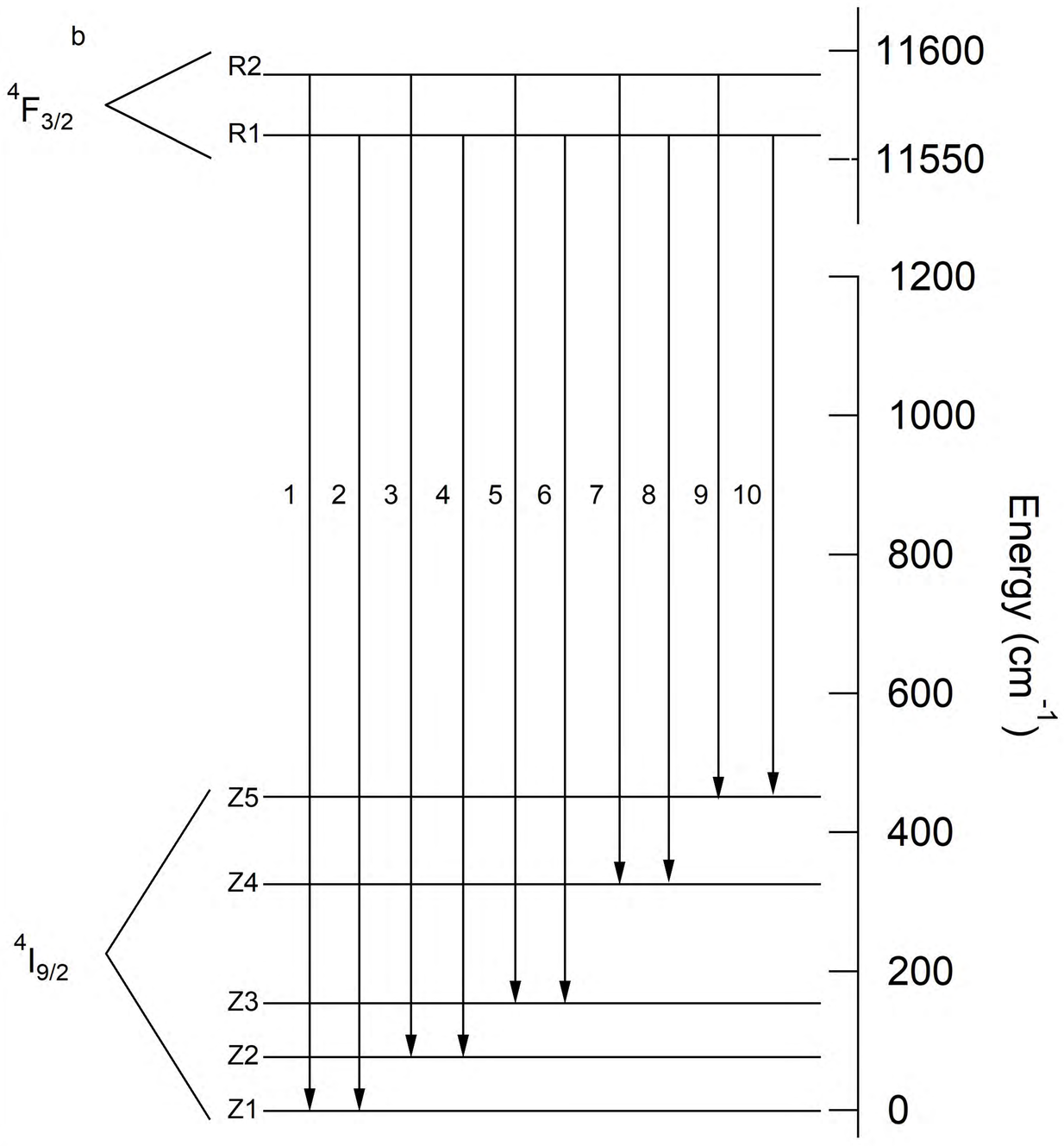

This is a preprint, the final version is subject to change, of the American Mineralogist (MSA)
Cite as Authors (Year) Title. American Mineralogist, in press.
DOI: https://doi.org/10.2138/am-2019-7011

Figure 5c

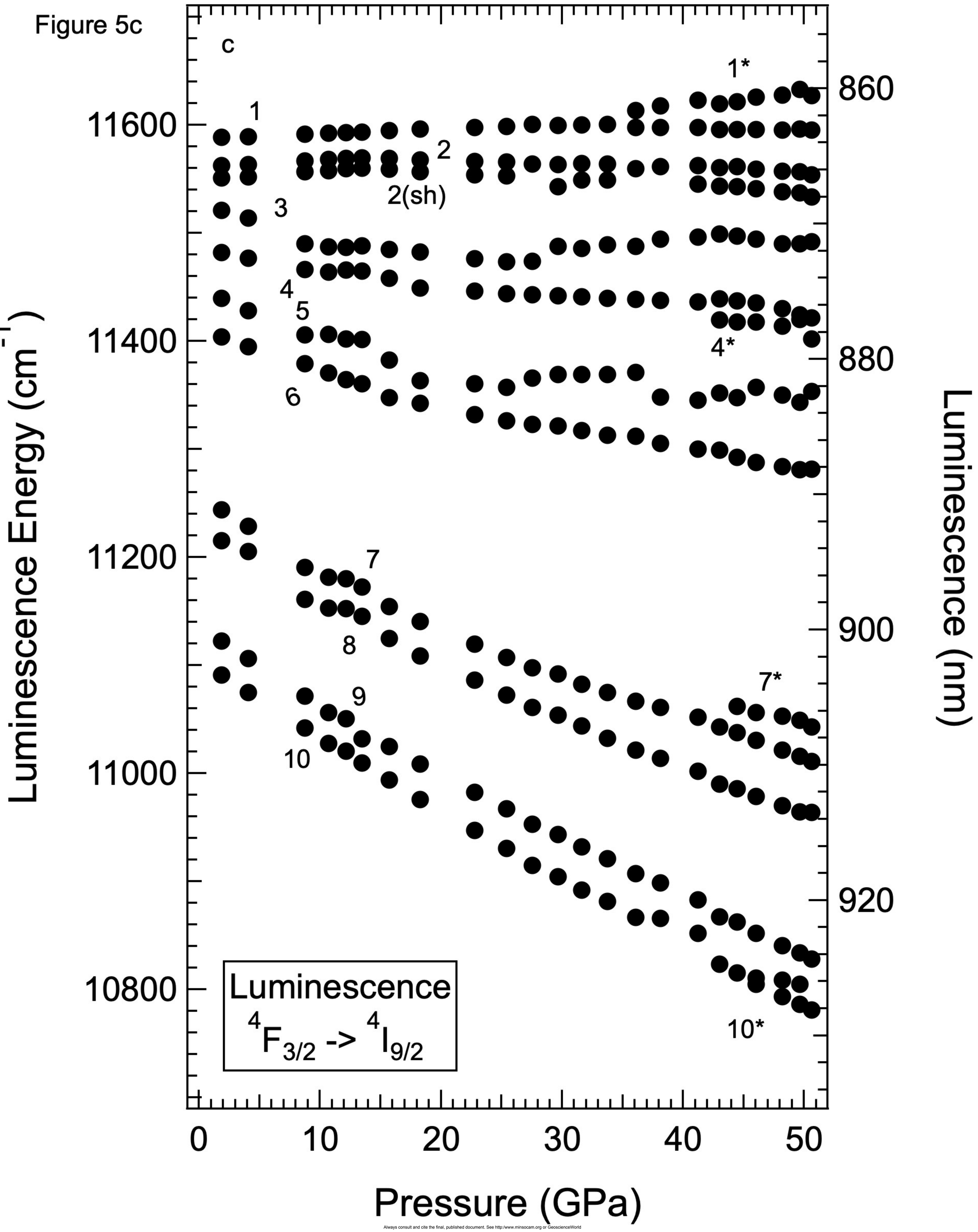

Figure 6ab

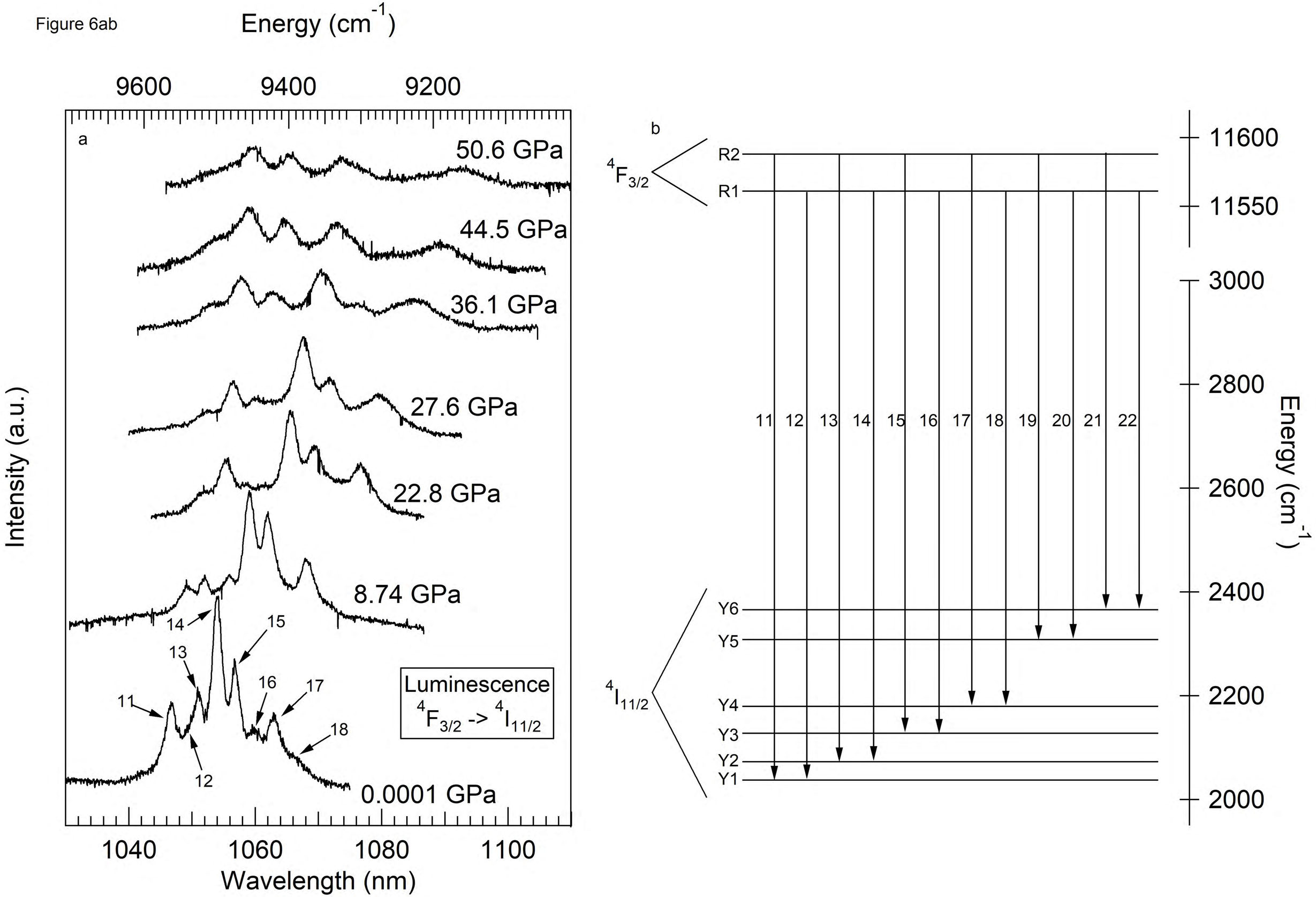

This is a preprint, the final version is subject to change, of the American Mineralogist (MSA)
Cite as Authors (Year) Title. American Mineralogist, in press.
DOI: https://doi.org/10.2138/am-2019-7011

Figure 6c

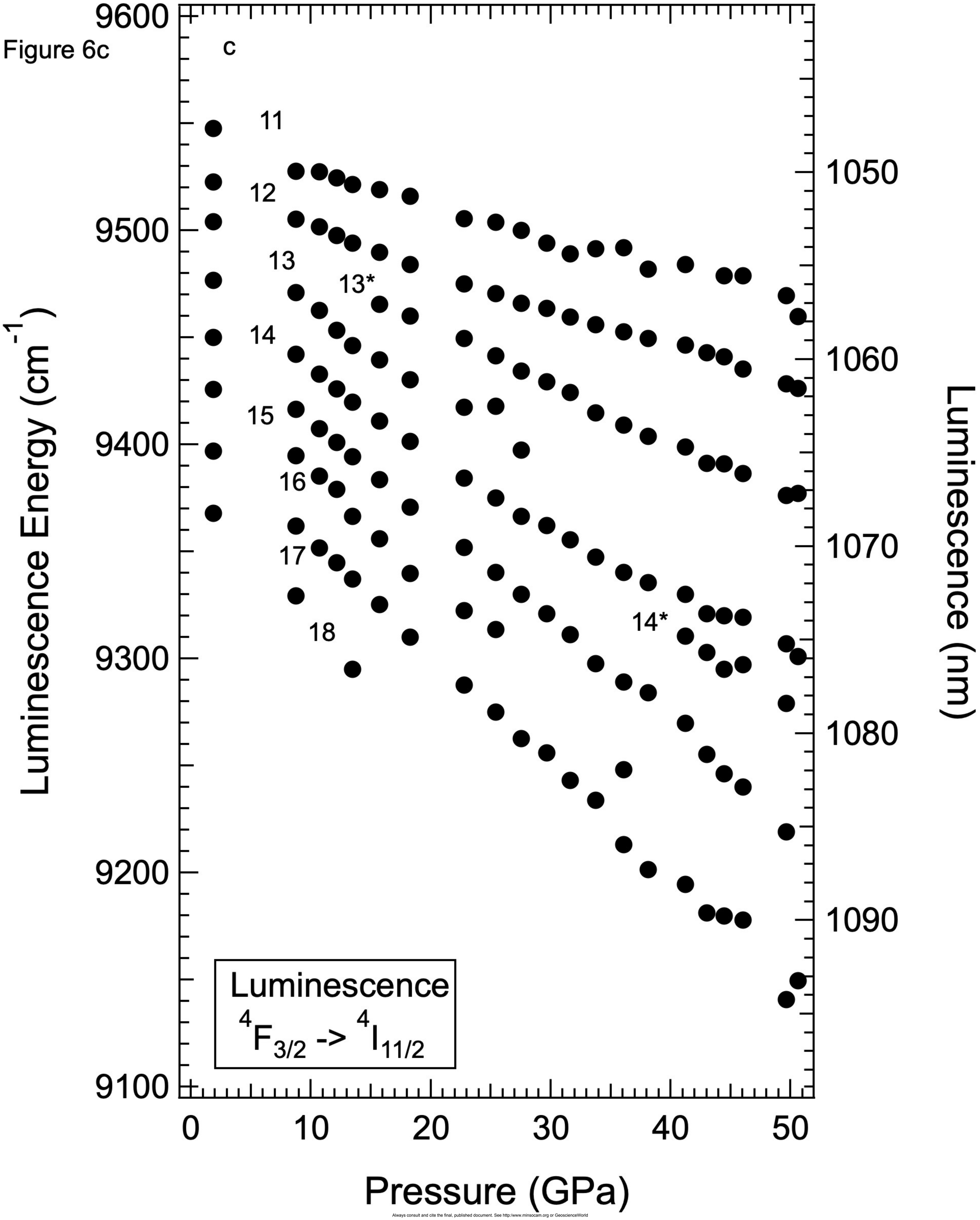

Figure 7ab

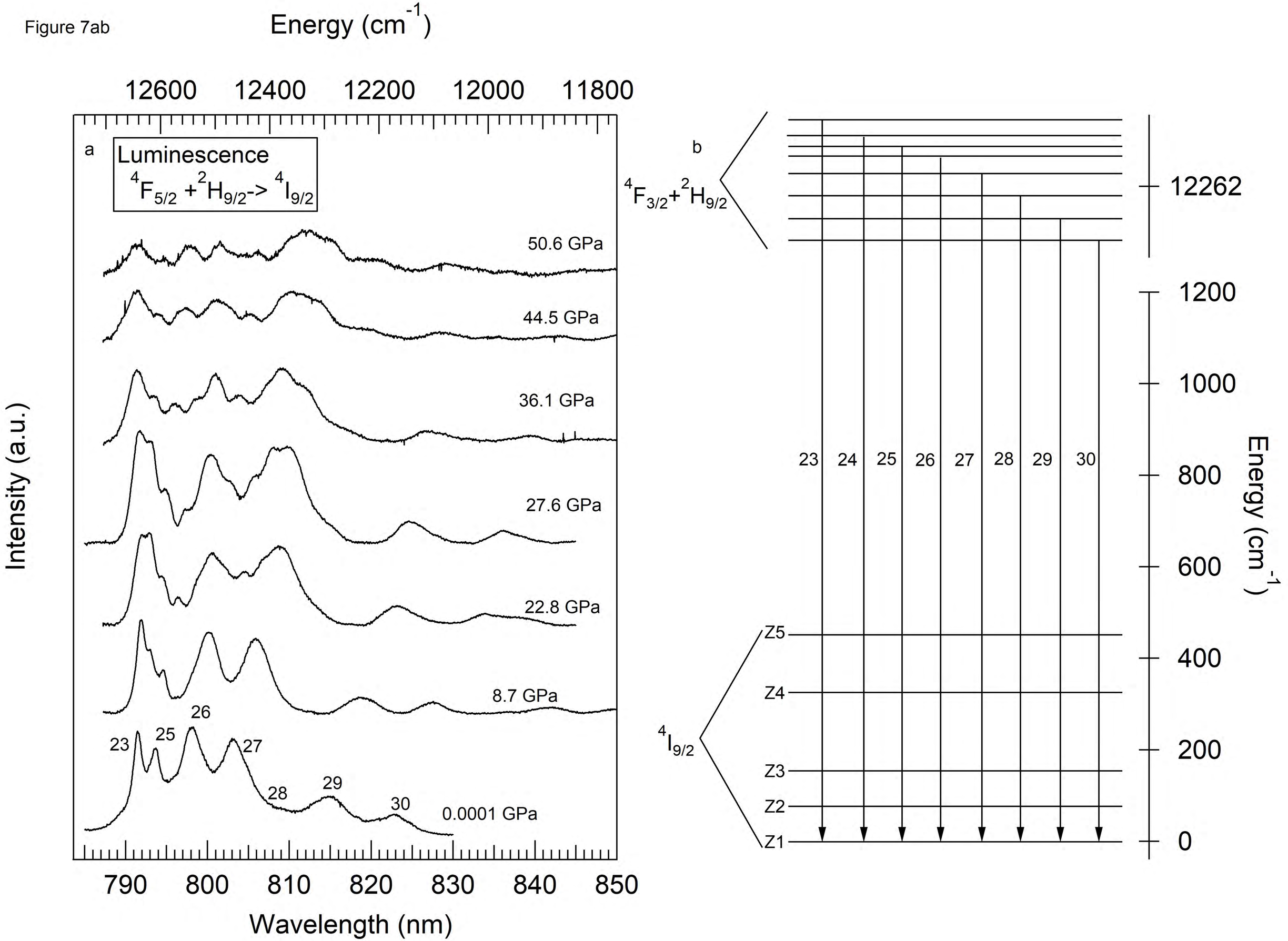

Figure 7c

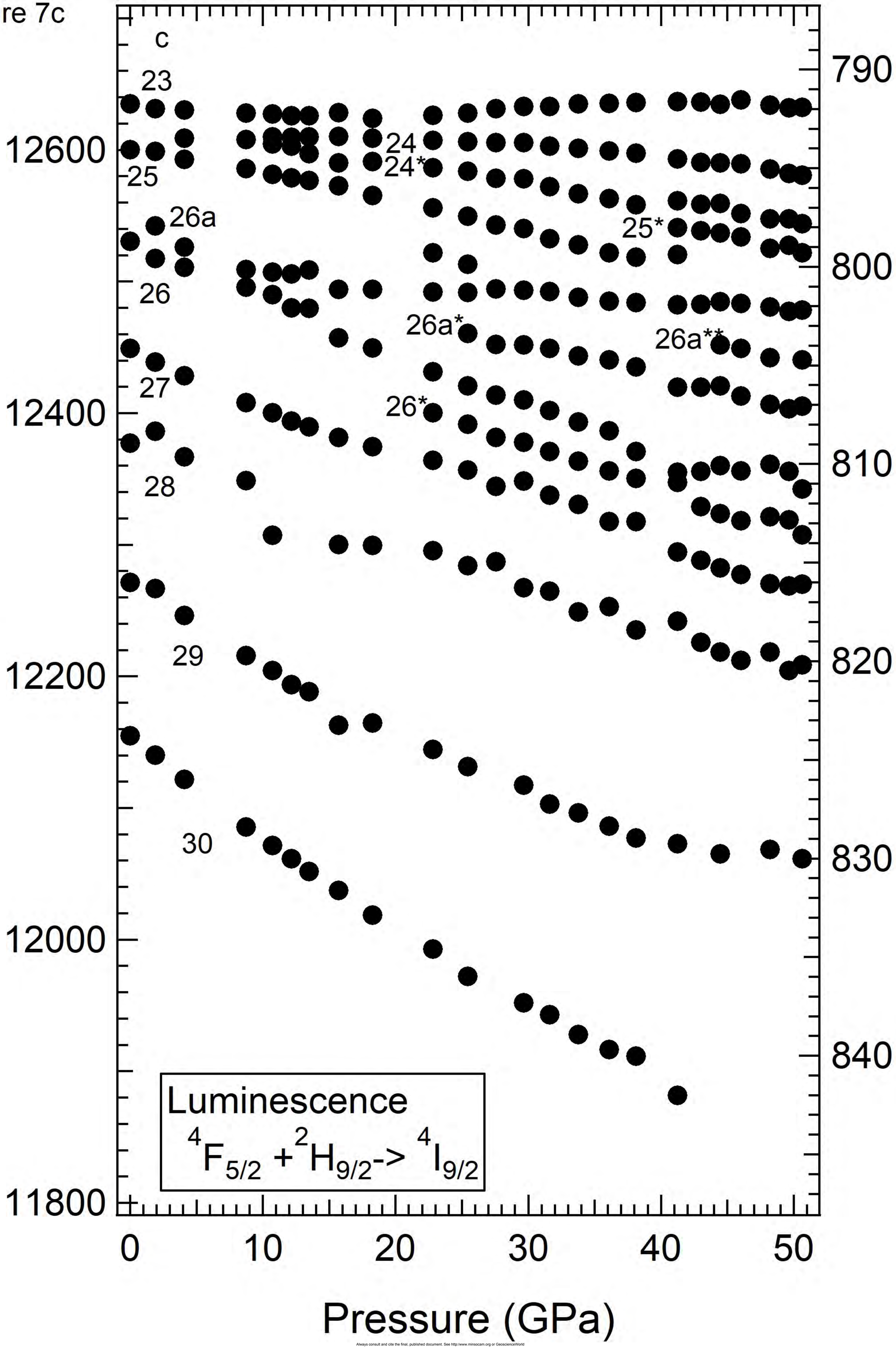

This is a preprint, the final version is subject to change, of the American Mineralogist (MSA)
Cite as Authors (Year) Title. American Mineralogist, in press.
DOI: https://doi.org/10.2138/am-2019-7011

Figure 8

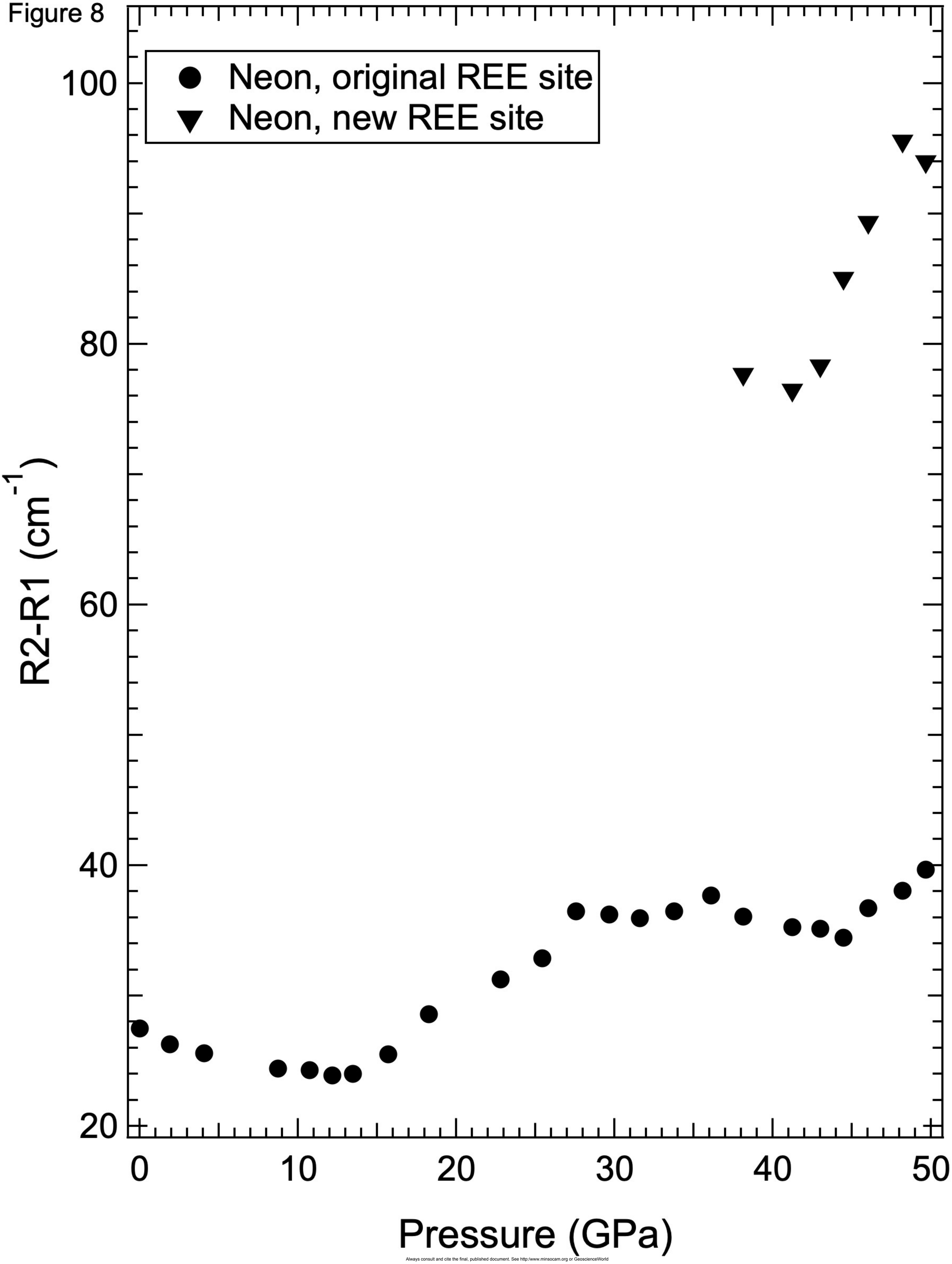

This is a preprint, the final version is subject to change, of the American Mineralogist (MSA)
Cite as Authors (Year) Title. American Mineralogist, in press.
DOI: https://doi.org/10.2138/am-2019-7011

Figure 9